DEVELOPMENTAL BIOLOGY

Glycolytic state of aortic endothelium favors hematopoietic transition during the emergence of definitive hematopoiesis

Anu PV[1], Shubham Haribhau Mehatre[1], Catherine M. Verfaillie[2], Mohammad Tauqeer Alam[3], Satish Khurana[1]*

The first definitive hematopoietic progenitors emerge through the process of endothelial-to-hematopoietic transition in vertebrate embryos. With molecular regulators for this process worked out, the role of metabolic pathways used remains unclear. Here, we performed nano–LC-MS/MS–based proteomic analysis and predicted a metabolic switch from a glycolytic to oxidative state upon hematopoietic transition. Mitochondrial activity, glucose uptake, and glycolytic flux analysis supported this hypothesis. Systemic inhibition of lactate dehydrogenase A (LDHA) increased oxygen consumption rate in the hemato-endothelial system and inhibited the emergence of intra-aortic hematopoietic clusters. These findings were corroborated using *Tie2-Cre*–mediated deletion of *Ldha* that showed similar effects on hematopoietic emergence. Conversely, stabilization of HIF-1α via inhibition of oxygen-sensing pathway led to decreased oxidative flux and promoted hematopoietic emergence in mid-gestation embryos. Thus, cell-intrinsic regulation of metabolic state overrides oxygenated microenvironment in the aorta to promote a glycolytic metabolic state that is crucial for hematopoietic emergence in mammalian embryos.

INTRODUCTION

In vertebrates, the hematopoietic system develops in multiple waves at different extra- and intraembryonic sites. The first wave of hematopoiesis occurs in yolk sac (YS) at embryonic day 7.5 (E7.5), giving rise to primitive erythroid-myeloid progenitors (*1*, *2*). The second wave marks the appearance of definitive hematopoietic stem cells (dHSCs) with multi-lineage, long-term repopulation capacity. The dHSCs are first formed in the dorsal aorta (DA) within the aorta-gonad-mesonephros (AGM) and associated major blood vessels by E10.5 (*3*). The hemogenic endothelium lining these vessels undergoes endothelial-to-hematopoietic transition (EHT) to give rise to HSCs (*4*). A number of physico-molecular changes during this trans-differentiation process lead to the appearance of intra-aortic hematopoietic clusters (IAHCs) (*5*). Now fairly well characterized for the molecular regulators involved and transitional cellular heterogeneity, this crucial event has been found to be conserved across vertebrate species (*6*–*9*). Runt-related transcription factor 1 (RUNX1) plays an important role in the emergence of hematopoietic progenitors in mid-gestation stage embryos (*10*). While endothelial deletion of *Runx1* blocked the emergence of hematopoietic progenitors, Vav1-Cre–mediated deletion showed only lineage-specific hematopoietic defects (*11*). Contrarily, GATA binding protein 2 (GATA2) was essential during EHT process, but its sustained expression was found to be the key to the maintenance of definitive hematopoietic activity (*8*). While it is unequivocally established that cell-extrinsic factors also affect cell fate decisions, understanding of these regulators in EHT process has been limited.

Along with the cellular and molecular players, physical attributes of the niche, such as pO_2, have been studied for their role in maintaining homeostasis. The oxygen-sensing mechanism plays a major role in regulating the cellular metabolic pathways and energy production (*12*). Through oxygen-dependent hydroxylase activity, prolyl-hydroxylase domain–containing proteins induce Von Hippel-Lindau tumor suppressor (VHL)–mediated proteasomal degradation of hypoxia-inducible factor–1α (HIF-1α), the master regulator of cellular response to hypoxia (*13*). Hypoxia-driven HIF-1α stabilization can increase glycolytic flux via transcriptional activation of several glycolytic enzymes, in addition to lactate dehydrogenase A (LDHA) involved in anaerobic glycolysis (*14*). HIF-1α also inhibits oxidative mitochondrial pathways via transcriptional activation of pyruvate dehydrogenase kinase (PDK) that inhibits catalysis of glycolytic product pyruvate to acetyl coenzyme A (CoA) (*15*). Stabilization of hypoxia pathway and the resulting glycolytic state has been shown to play a decisive role in adult HSC function (*16*, *17*). Notwithstanding the micro-niches the HSCs occupy and the availability of oxygen within the bone marrow (BM), it has been comprehensively documented that the primitive HSCs use glycolytic means for energy production (*18*, *19*). The loss of LDHA decreased glycolytic flux for oxidative pathways and increased the accumulation of ROS resulting in functional decline (*20*). Similarly, the deficiency of PDK that led to an increased oxidative metabolic flux abrogated HSC function (*17*). Expectedly, HSCs deficient in *Hif-1α* entered cell cycle and showed poor function and faster exhaustion following hematopoietic stress (*21*). Hence, it has been established that hypoxia pathway leading to glycolytic metabolism for energy production plays a crucial role in maintaining the quiescence of adult BM HSCs. In the case of hematopoietic development, also, the involvement of hypoxia pathway has been elucidated. Using hydroxyprobe labeling, hypoxic nature of embryonic hematopoietic sites in aorta, placenta, and fetal liver (FL) was demonstrated (*22*). This study showed that VEC-Cre–mediated deletion of *Hif-1α* led to decrease in the emergence of hematopoietic progenitors in aorta. Notwithstanding, the link between the hypoxia pathway and then metabolic state of the embryonic and fetal hematopoietic progenitors remained unclear. We earlier reported the differences in energy-producing metabolic pathways between the FL and adult BM-derived HSCs (*23*). These

[1]School of Biology, Indian Institute of Science Education and Research Thiruvananthapuram, Maruthamala PO, Vithura, Thiruvananthapuram 695551, Kerala, India. [2]Inter-departmental Stem Cell Institute, KU Leuven, 3000 Leuven, Belgium. [3]Department of Biology, College of Science, United Arab Emirates University, Al-Ain, UAE.
*Corresponding author. Email: satishkhurana@iisertvm.ac.in

studies showed that, unlike adult HSCs, higher levels of mitochondrial respiration and faster adenosine 5′-triphosphate (ATP) production fuel proliferative fetal HSCs. Increased oxidative flux in adult HSCs has been linked with enhanced ROS levels and associated DNA damages, leading to functional decline (*24*). Our recent studies showed that a better DNA damage response in fetal HSCs might be central to the tolerance to proliferative stress (*25*). As dHSCs first appear in the lumen of large blood vessels, the oxygenation status of the microenvironment and resulting metabolic adaptations are of relevance to the EHT process. Recent findings have associated metabolic changes with the initiation of blood circulation. Single-cell transcriptomic analysis predicted a metabolic change with decrease in glycolysis as hematopoietic lineage commitment commenced (*26*). Deletion of *Ncx1* that leads to failure in setting up of heartbeat and blood circulation, blocked this metabolic switch, and inhibited hematopoietic maturation. However, evidence for the involvement of metabolic state in the trans-differentiation that happens during EHT has been elusive.

In the present study, we performed nano–liquid chromatography–tandem mass spectrometry (LC-MS/MS)–based proteomic analysis to understand the molecular program involved in the transition of endothelial to hematopoietic cells (HCs). Proteomics data supported by extracellular flux analysis strongly suggested a metabolic switch from glycolytic to oxidative means of energy production as endothelial cells (ECs) acquired hematopoietic fate. We use pharmacologic and genetic means to establish that the glycolytic state of ECs was critical for the lineage transition. Systemic inhibition or EC-specific deletion of *Ldha* decreased glycolytic flux, leading to contraction in hematopoietic emergence in aorta. We could perform gain-of-function studies for glycolytic pathway via inhibition of oxygen-sensing mechanism, wherein increased glycolytic flux increased hematopoietic emergence.

RESULTS

Proteomic profiling of cells transitioning from endothelial to hematopoietic lineage

To understand the involvement of metabolic pathways in specific stages of EHT, we aimed at performing proteomic analysis of the cells transitioning from the endothelial to hematopoietic fate. The cells in different stages of EHT were isolated from E10.5 mouse embryos. The ECs ($CD31^+$c-kit^-), hemogenic ECs (HECs; $CD31^+$c-kit^+), and hematopoietic progenitors (HCs; $CD31^-$c-kit^+) were isolated by fluorescence-activated cell sorting (FACS) (Fig. 1A). The efficiency of the antibodies used to isolate these cell populations in different stages of trans-differentiation was confirmed using whole-mount immunostaining of E10.5 embryos (fig. S1). Fluorophore-conjugated anti-mouse CD31 and anti-mouse c-kit antibodies were used to detect ECs, HECs, and HCs within the dorsal aorta. Results clearly showed labeling of specific cell types (fig. S1, bottom). Thereafter, we used these antibodies to FACS sort the three populations in addition to the double-negative cells (DNCs; $CD31^-$c-kit^-) that were used for comparison. The lysate from the sorted cells was thermally denatured, reduced, and alkylated. Trypsin-digested samples were desalted and analyzed on nano-LC platform directly connected to a mass spectrometer (Fig. 1B). Following protein identification of 2109 proteins and quantification using Proteome Discoverer program, computational analysis was performed on the global protein expression to examine the molecular pathways enriched in each cell population. To examine the overall difference between the proteomic profile of the cells in different stages of EHT, we first performed principal components analysis using three biological replicates ($n = 3$) for each cell type based on the mean values from three technical replicates for each sample ($N = 3$) (Fig. 1C). Replicates of each cellular proteome clustered together with clear separation between the cells in distinct differentiation stages. The DNC and HEC populations showed clear separation from the EC and HC populations that were placed unexpectedly closer. Followed by this, a heatmap using the entire dataset was created to visualize the abundance of individual proteins in different samples (Fig. 1D). Hierarchical clustering of the samples on heatmap also confirmed the resemblance of overall proteomic profiles of EC and HC populations. The proteins differentially expressed between different pairs of cell populations were then used for Venn diagram analysis (Fig. 1, E and F). For this analysis, we used proteins that were up-regulated (Fig. 1E) or down-regulated (Fig. 1F) with fold change of >2 and P value of <0.05. As noted from the hierarchical clustering analysis, we found a higher number of proteins differentially expressed between HC versus HEC (957 proteins) and HEC versus EC (1023 proteins) than between HC versus EC (504 proteins) populations. Results differed modestly when we compared the numbers of up-regulated (Fig. 1E) and down-regulated proteins (Fig. 1F) between different sets of cell populations. To highlight the proteins differentially expressed in the cells at progressive stages of EHT, we plotted $\log_2$ fold change against the corresponding $-\log_{10}$ adjusted P values. Volcano plots were analyzed for each pair of cell populations, namely, HC versus EC (Fig. 1G), HC versus HEC (Fig. 1H), and HEC versus EC (Fig. 1I). For each comparison, differentially expressed proteins with fold change of >2 and P value of <0.05 were highlighted.

Hematopoietic transition from endothelial lineage involves a metabolic switch to mitochondrial pathways

Next, we aimed at identifying the candidate pathways involved in the process of trans-differentiation from endothelial to hematopoietic lineage. We used the list of differentially expressed proteins, identified for each cell population to perform pathway enrichment analysis using Reactome database. Venn diagram analysis was performed for the pathways differentially expressed between each pair of cell populations, namely, ECs, HECs, and HCs with P value of <0.05 (Fig. 2, A and B). Both, up-regulated (Fig. 2A) and down-regulated (Fig. 2B) pathways between different pairs of cell population showed a high level of exclusivity with hardly any pathways commonly up-regulated or down-regulated between different stages of trans-differentiation. The differentially expressed pathways up-regulated ($P < 0.05$) between HC versus EC (Fig. 2C), HC versus HEC (fig. S2A), and HEC versus EC (fig. S2B) populations and down-regulated ($P < 0.05$) between HC versus EC (Fig. 2C), HC versus HEC (fig. S2C), and HEC versus EC (fig. S2D) populations were identified. To identify the candidate pathway/s involved in the EHT process, we focused on the two terminal differentiation stages during this trans-differentiation process. Comparison of HC and EC populations for differentially enriched pathways presented interesting results (Fig. 2C). Among the 830 detected pathways, 17 pathways were significantly enriched in the HC population. We observed that the cellular processes involved in complex I biogenesis and respiratory electron transport were represented significantly higher in HCs in comparison to that in the ECs. Heatmap analysis of the proteins

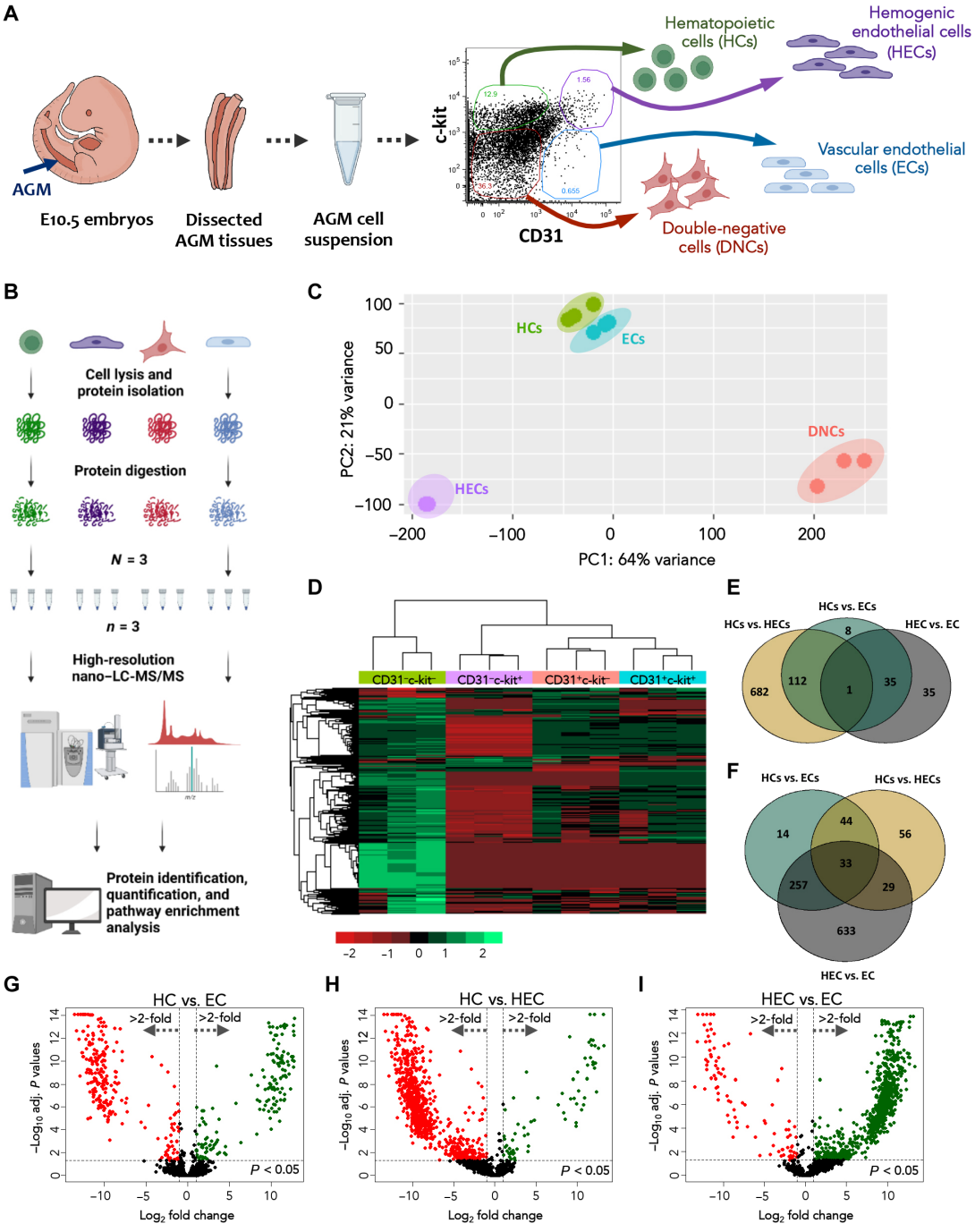

Fig. 1. Proteomic analysis of AGM cells undergoing EHT. (**A**) Experimental scheme depicting the protein extraction and mass spectrometric analysis of the aortic cells in the process of EHT. AGM from E10.5 embryo is sub-dissected to harvest the aortic tissues followed by collagenase mediated mild dissociation to get a single-cell suspension. The HCs ($CD31^{-}c\text{-}kit^{+}$ cells), HECs ($CD31^{+}c\text{-}kit^{+}$ cells), ECs ($CD31^{+}c\text{-}kit^{-}$ cells), and DNCs ($CD31^{-}c\text{-}kit^{-}$ cells) were isolated by fluorescence-activated cell sorting (FACS). (**B**) The cells lysed by sonication were reduced and alkylated before trypsinization and desalting. Trypsinized peptides were analyzed by label-free nano–LC-MS/MS followed by bioinformatic analysis ($n = 3$, $N = 3$). (**C**) Principal components analysis was performed on untargeted proteomic profiles of HC, HEC, EC, and DNC samples from AGM tissues of E10.5 embryos. PC, principal component. (**D**) Hierarchical clustering of differentially expressed proteins detected and quantified by MS. (**E**) Venn diagram analysis of the proteomes detected from the ECs, HECs, and HCs. The number of proteins commonly or exclusively up-regulated between each pair (HCs versus HECs, HCs versus ECs, and HECs versus ECs) of cell populations is shown. (**F**) Venn diagram analysis of proteins commonly or exclusively down-regulated between each pair (HCs versus HECs, HCs versus ECs, and HECs versus ECs) of cell populations was shown. Volcano plots showing proteins differentially expressed between (**G**) HC versus EC, (**H**) HC versus HEC, and (**I**) HEC versus EC populations. Log_2 fold change and $-log_{10}$ adjusted P values are plotted on the x and y axes, respectively. Represented data are based on three independent biological replicates ($n = 3$), each with three technical replicates ($N = 9$). Red dots represent proteins with statistically significant ($P < 0.05$) higher abundance of >2 fold change. Green dots represent proteins having statistically significant ($P < 0.05$) lower abundance with >2 fold change.

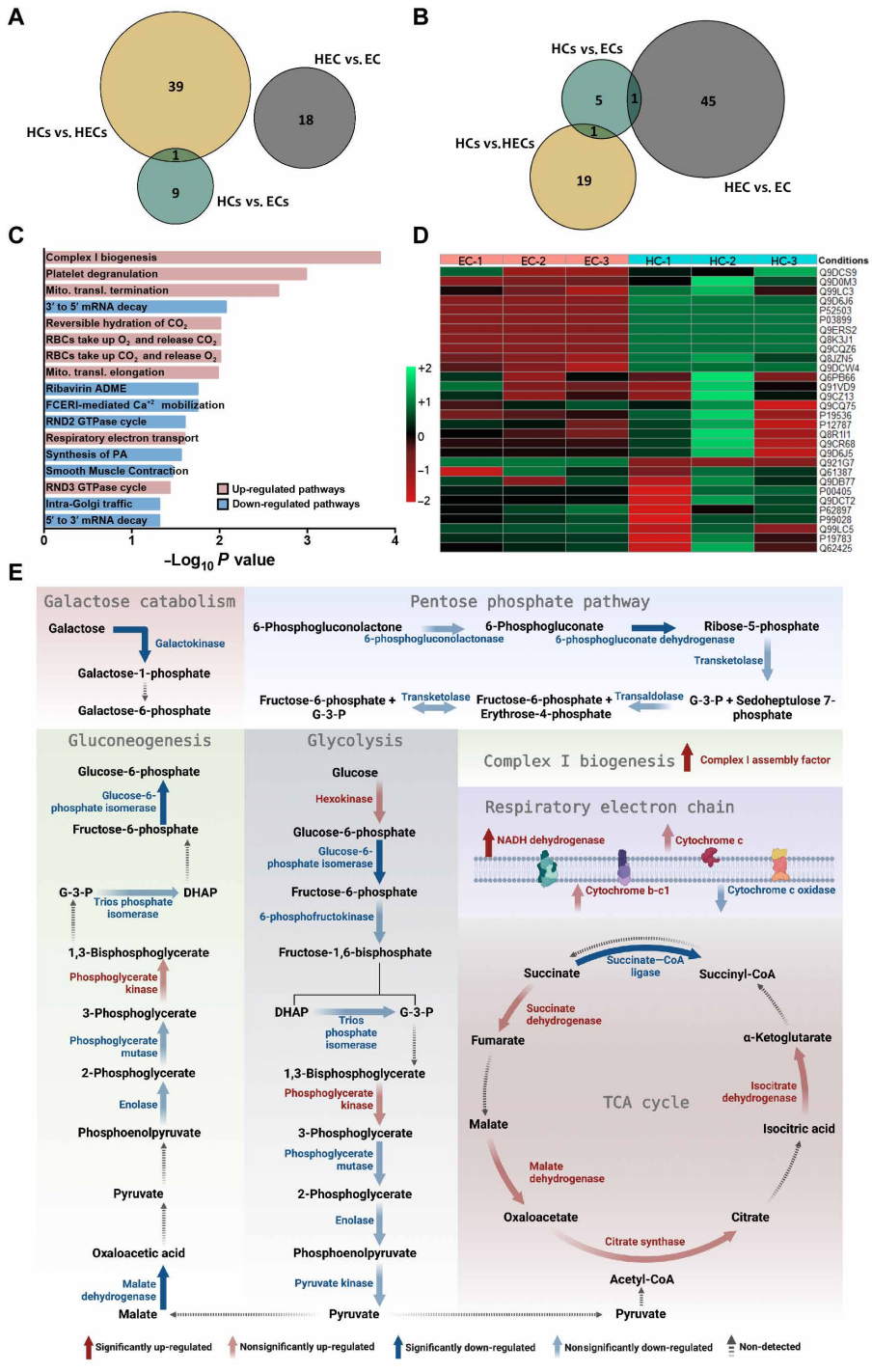

Fig. 2. Proteomic profile predicts a metabolic switch from glycolytic to oxidative respiration during EHT process. (**A**) Venn diagram analysis of the pathways enriched in EC, HEC, and HC populations. The number of pathways commonly or exclusively up-regulated between each pair (HCs versus HECs, HCs versus ECs, and HECs versus ECs) of cell populations is shown. (**B**) Venn diagram analysis of pathways commonly or exclusively down-regulated between each pair (HCs versus HECs, HCs versus ECs, and HECs versus ECs) of cell populations. (**C**) Reactome pathway analysis of global differentially enriched pathways with a *P* value of <0.05. Both significantly up- and down-regulated pathways in HCs versus ECs are illustrated. RBCs, red blood cells; GTPase, guanosine triphosphatase. (**D**) Heatmap illustrating the proteins involved in significantly altered metabolic pathways between HCs and ECs, namely, the respiratory electron transport chain and complex I biogenesis. (**E**) Model depicting key changes in the energy-producing metabolic pathways during hematopoietic lineage commitment from aortic endothelium. Enrichment status of various enzymes involved in galactose catabolism, gluconeogenesis, glycolysis, pentose phosphate pathway, tricarboxylic acid (TCA) cycle, complex I biogenesis and respiratory electron transport in HCs versus ECs has been illustrated. Color codes for changes upon hematopoietic commitment from endothelial fate are shown in the figure. Enzymes not detected in the proteomic profile are represented as broken arrows. The schematic was created via BioRender.

included in these cellular processes confirmed the findings and identified several key proteins enriched in the HCs (Fig. 2D). With hematopoietic lineage commitment, we also observed a decrease in the enrichment of several of the glycolytic enzymes, such as glucose-6-phosphate isomerase, 6-phosphofructokinase, enolase, and pyruvate kinase. To expand our observations on broader energy-producing metabolic pathways, we included cellular process that was differentially represented between ECs and HCs, nonsignificantly (fig. S3A). We could notice that glycolysis pathway was enriched in the EC population in comparison to that in the HC population ($P > 0.05$). Subsequently, we explored the enrichment levels of the detected proteins that belonged to these pathways (fig. S3B). Among these proteins, we focused on the proteins relevant to the metabolic status of the cells and were differentially expressed between HCs versus ECs with $P < 0.05$ (fig. S3C). We noted that several proteins that assist in increasing glucose levels or other glycolytic intermediates were also enriched in the EC population. These include galactokinase enzyme that mediates galactose catabolism contributing to glycolytic pathway (Fig. 2E and fig. S3C). This was also reflected in the down-regulation of the galactose catabolism pathway in HCs (Fig. 2E and fig. S3A). Gluconeogenesis that acts as an alternative source of glucose was also represented at a higher level in EC cells, albeit nonsignificantly (fig. S3A and Fig. 2E). Malate dehydrogenase and glucose-6-phosphate isomerase enzymes that mediate gluconeogenesis pathway showed a notable decrease with hematopoietic lineage commitment (fig. S3B and Fig. 2E). Others, such as enolase, phosphoglycerate mutase, and trios-phosphate isomerase, showed a lower enrichment in HCs in comparison to that in ECs (Fig. 2E and fig. S3C). Primarily working as a catabolic pathway, pentose phosphate pathway (PPP) acts as a source of reduced form of nicotinamide adenine dinucleotide phosphate for glycolytic processes (*27*). 6-Phosphogluconate dehydrogenase that mediates PPP was also enriched in ECs (Fig. 2E and fig. S3B). Apart from these, several other enzymes from this pathway showed a nonsignificant decrease in enrichment status in the HCs (Fig. 2E and fig. S3C). Succinate-CoA ligase, an important regulator of the tricarboxylic acid cycle was significantly down-regulated, indicative of a possible increased flux. As several of these pathways, especially gluconeogenesis, galactose catabolism, and PPP, have also their involvement in oxidative pathways, these results warranted a more detailed analysis of the metabolic state of the cells undergoing EHT. Notwithstanding, in silico analysis of the proteomics data from the cells undergoing EHT pointed toward an increase in the mitochondrial respiratory pathways at the expense of glycolytic flux in HCs. These observations are indicative of a metabolic switch in corroboration of the earlier findings made using the transcriptomics data from the cells (*26*).

Switch from glycolytic to oxidative pathways coincides transition of endothelial to hematopoietic fate

On the basis of proteomic analysis of the cells undergoing EHT, we hypothesized that the ECs undergo a metabolic switch to a highly oxidative mode. Before examining the importance of these pathways in the hematopoietic emergence, we first aimed at confirming whether the metabolic state of the ECs changed as they transition into hematopoietic lineage. As the proteomic profile indicated an increased mitochondrial respiratory rate, we queried whether the cells in progressive stages of EHT differed in the mitochondrial content and activity. We used probes to quantify the mitochondrial mass and membrane potential of the cell populations identified by immunostaining followed by flow cytometry (fig. S4A). The cells identified as EC and HC populations were labeled for MitoTracker Green (Fig. 3A) and MitoTracker Red CMXRos (Fig. 3B) for total and active mitochondria, respectively. Analysis of the total mitochondrial content presented unexpected results as we noted significantly higher mitochondrial content in ECs than that in HCs (Fig. 3A). However, the active mitochondrial content showed a marked increase as the ECs trans-differentiated into the hematopoietic lineage (Fig. 3B). These results were validated by quantifying mitochondrial reactive oxygen species (ROS) levels via staining with MitoSOX Red (Fig. 3C). A clear increase in the mitochondrial ROS production was noted in HC than EC population. We followed these experiments with flow cytometry–based examination of glucose uptake by ECs in comparison to HCs (Fig. 3D). We used fluorescent glucose analog 2-[*N*-(7-nitrobenz-2-oxa-1,3-diazol-4-yl) amino]-2-deoxy-D-glucose (2-NBDG). The results showed a clear difference between the two cell types, where ECs showed a significantly higher fluorescence due to 2-NBDG uptake (Fig. 3D). We followed this with examining the expression of the most efficient glucose transporter GLUT3 by flow cytometry. Analysis of its expression showed a significantly higher level in ECs than in the HC population of the dissected AGM tissue (Fig. 3E). Upon analysis of the proteomics data from the cells undergoing EHT, we noticed that only GLUT1 was detected among all the glucose transporters and was expressed at higher levels in ECs. To confirm these observations, we performed flow cytometry analysis to examine the expression of GLUT1 using specific antibodies along with immunostaining for c-kit and CD31. Comparison of mean fluorescence intensity (MFI) for GLUT1 signals confirmed a significantly higher expression levels in ECs than that in HCs (Fig. 3F). We also performed whole-mount immunostaining of control E10.5 embryos to analyze GLUT1 expression in IAHCs within the DA (Fig. 3G). Qualitative analysis of the images showed a clear overlapping of GLUT1 and CD31 signals in the IAHCs (marked by dotted lines) with lower levels in c-kit–expressing non-ECs (marked by arrowheads). For some of the proteins that are important for glycolytic state of the cells and were not detected in our proteomics data, we performed gene expression analysis by quantitative reverse transcription polymerase chain reaction (PCR) (fig. S4, B to G). While several of them, such as hexokinase 1 (*Hk1*; fig. S4B), *Ldha* (fig. S4C), phosphofructokinase (*Pfk*; fig. S4F), and pyruvate dehydrogenase E1 alpha 1 (*Pdha1*; fig. S4G), showed no change, we found the expression of *Pdk* (fig. S4D) and *Glut1* (fig. S4E) to be significantly higher in ECs in comparison to that in HCs. Overall, these experiments supported the hypothesis generated from the proteomics data that the EHT process involves a metabolic switch. We then enquired whether the proteomic profile, coupled with the mitochondrial function and glucose uptake analysis, accurately represented the status of glycolytic and mitochondrial metabolism in these cells. To this end, we aimed at bioenergetic profiling of the FACS-sorted EC ($CD31^+c\text{-}kit^-$), HEC ($CD31^+c\text{-}kit^+$), and HC ($CD31^-c\text{-}kit^+$) populations using Seahorse XFp (Agilent) extracellular flux analyzer. We chose to perform analysis for the extracellular acidification rate (ECAR) on FACS-sorted cell populations at different stages of EHT. The results showed a clear decrease in the glycolytic ECAR in HECs and HCs when compared to that in the ECs (Fig. 3H and fig. S4, H and I). The glucose-induced glycolytic rate in HECs and HCs also remained significantly lower than in the ECs (fig. S4J). Similar observations were made for maximal glycolysis, measured by the addition of ATP synthase inhibitor

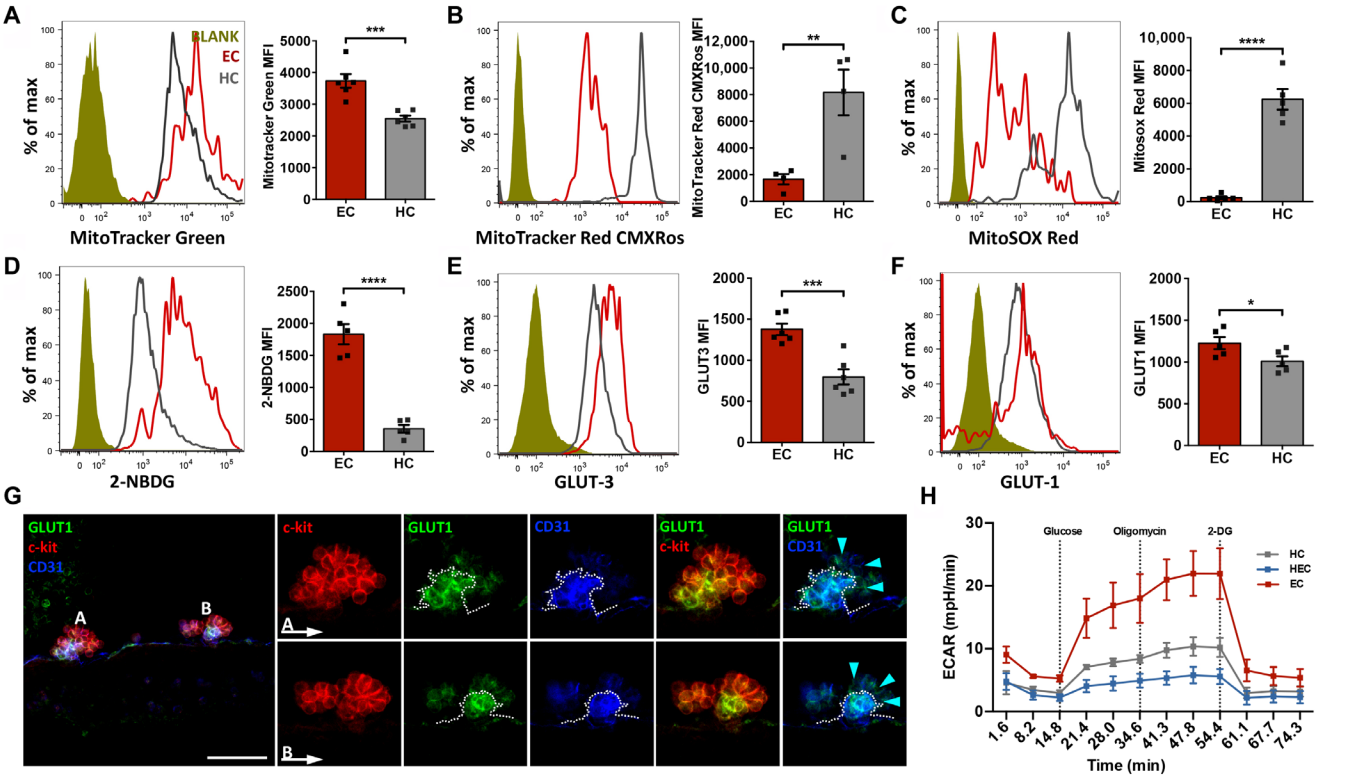

Fig. 3. Lower mitochondrial function and increased glucose uptake support the glycolytic state of aortic ECs. (**A**) Flow cytometry–based quantification of total mitochondria in E10.5 AGM-derived EC and HC populations. The cells were immunolabeled with antibodies against CD31 and c-kit along with MitoTracker Green. Cells gated for EC ($CD31^+$c-kit^-) and HC ($CD31^-$c-kit^+) populations were further analyzed for MitoTracker Green fluorescence. Representative histograms along with mean fluorescence intensity (MFI) values for MitoTracker Green are shown. (**B**) Quantification of active mitochondrial content based on MitoTracker Red CMXRos intensity in ECs and HCs. (**C**) Mitochondrial ROS content analyzed in ECs and HCs by MitoSOX Red staining along with immunostaining for endothelial and hematopoietic markers. (**D**) Comparison of glucose uptake between ECs and HCs using fluorescent glucose analog 2-[*N*-(7-nitrobenz-2-oxa-1,3-diazol-4-yl) amino]-2-deoxy-D-glucose (2-NBDG). (**E**) Immunostaining for GLUT3 expression in EC and HC populations. Fluorophore-conjugated antibodies against CD31, c-kit, and GLUT3 were used for cell surface staining of cells derived from E10.5 AGM tissues. (**F**) Representative flow cytometry plots for GLUT1 expression in AGM-derived ECs and HCs identified by immunostaining for CD31 and c-kit. MFI values are provided for five biological replicates. Data represented in (A) to (F) are based on $n = 3$ to 4 and $N = 5$ to 6. (**G**) Whole-mount confocal images for GLUT1 expression in IAHCs within the embryonic aorta. Dotted line marks the IAHC area with CD31 expression overlapping high expression of GLUT1. Arrowheads indicate IAHC areas with $CD31^{lo/-}$ cells with lower expression of GLUT1. $n = 2$. Scale bar, 50 μm. (**H**) Extracellular flux analysis of FACS-sorted ECs ($CD31^+$c-kit^-), HECs ($CD31^+$c-kit^+), and HCs ($CD31^-$c-kit^+) from AGM tissues of mid-gestation embryos. Extracellular acidification rate (ECAR) was analyzed using Seahorse XFp glycolysis stress test in the three populations ($n = 3$ to 4). For all panels, data are presented as means ± SEM. Nonsignificant (ns) indicates $P > 0.05$; $^*P < 0.05$, $^{**}P < 0.01$, $^{***}P < 0.001$, and $^{****}P < 0.0001$ by two-tailed unpaired *t* test.

oligomycin (fig. S4K) and glycolytic reserve (fig. S4L). These differences upon hematopoietic commitment of ECs to HCs continued as the cellular loss of endothelial marker (fig. S4, J to L). These results clearly established that the aortic ECs are highly glycolytic in nature and achieve higher mitochondrial function during hematopoietic transition. Hence, the metabolic switch coincided with the lineage transition during the trans-differentiation process.

Pharmacologic inhibition of glycolysis abrogates EHT

The findings from the proteomics data, coupled with the analysis of mitochondrial and metabolic status of cells undergoing EHT, showed a switch from glycolytic to oxidative state. We next examined how crucial these respective metabolic states were in this lineage transition. We first used pharmacologic approach to inhibit the anaerobic glycolytic processes using LDHA inhibitor sodium oxamate (NaOX; 300 mg/kg). As a structural analog of pyruvate, it inhibits anaerobic processing of pyruvic acid to produce lactic acid, resulting in an increased mitochondrial function (*28*). Timed mating experiments were performed, and E9.5 pregnant dams were used for NaOX treatment, given intraperitoneally. Embryos were harvested at E10.5 for the analysis of hematopoietic emergence using whole-embryo staining, followed by confocal microscopy–based deep issue imaging (schematic in Fig. 4A). First, we examined whether NaOX treatment of the pregnant dams was sufficient to induce metabolic change in the AGM tissue. For this purpose, we performed ECAR analysis on the FACS-sorted EC and HC population from dissected AGM tissues. We observed a significant decrease in the glycolytic flux in the ECs from NaOX-treated embryos (Fig. 4, B and C), with no effect on glycolytic capacity and glycolytic reserve (fig. S5, A to C). However, we did not observe any significant change in the ECAR in HC fraction of the cells (fig. S5D). LDHA has been shown to induce a metabolic switch from a glycolytic state to a more oxidative

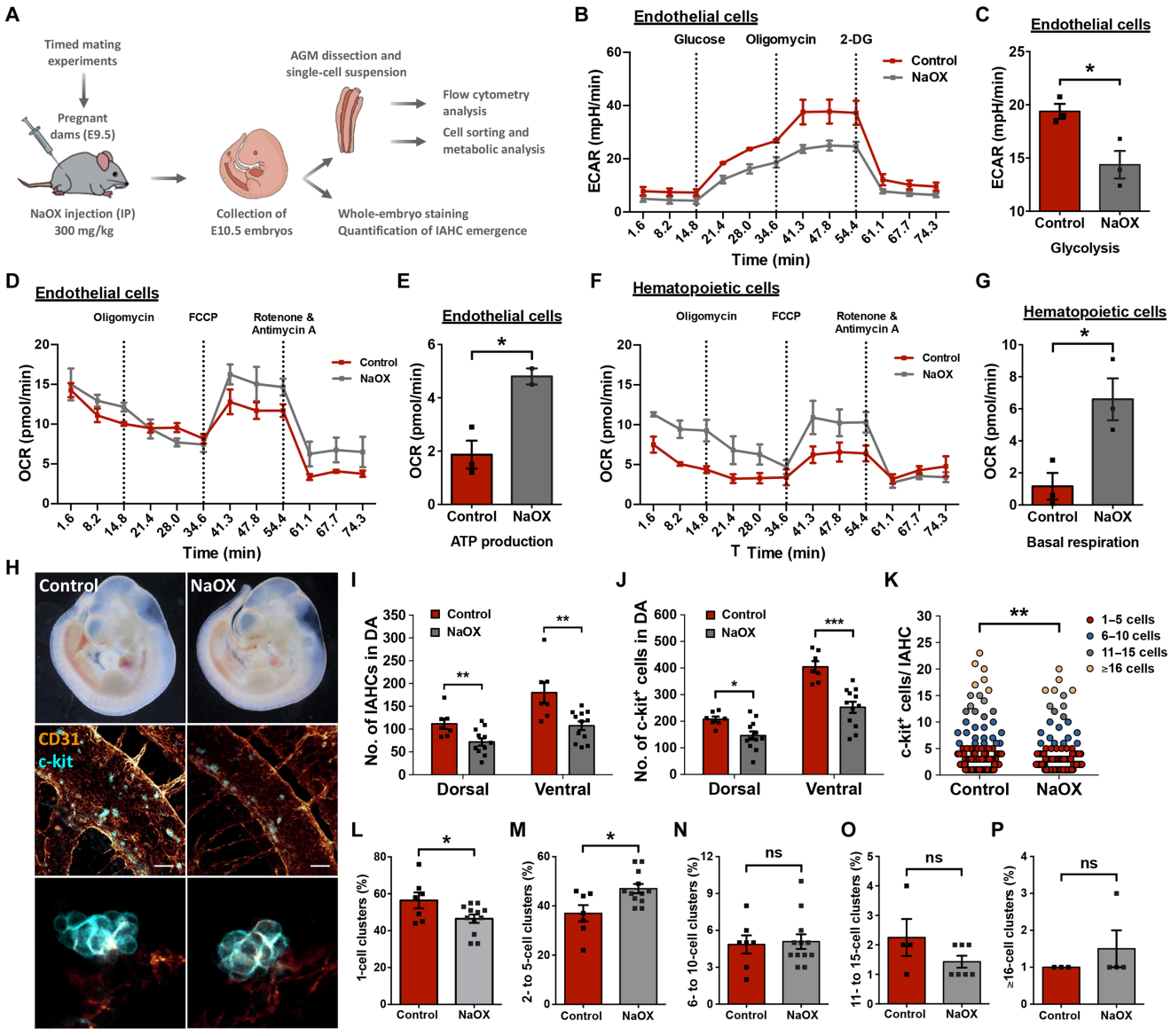

Fig. 4. LDHA inhibition impairs EHT. (**A**) Schematic showing the experimental design to understand the effect of LDHA inhibitor NaOX on the metabolic state and hematopoietic emergence in mid-gestation stage embryos. IP, intraperitoneal. (**B**) Glycolytic stress test performed to examine ECAR in ECs after NaOX treatment. (**C**) Effect of NaOX treatment on the glycolytic rate in sorted aortic ECs. (**D**) Mito stress test performed to examine OCR in sorted aortic ECs. FCCP, carbonyl cyanide *p*-trifluoromeoth oxyphenylhydrazone. (**E**) Comparison of ATP production calculated from mito stress test performed on aortic ECs from control and NaOX-treated embryos. (**F**) Quantification of OCR in HCs by mito stress test. (**G**) Comparison of basal respiration in sorted HCs from embryos with or without NaOX treatment. (**H**) Representative images from IAHC analysis of control and NaOX-treated E10.5 embryos using whole-mount immunofluorescence imaging. Top panel shows dark-field images; middle and bottommost (zoomed-in) panels shows immunofluorescence images captured for CD31 and c-kit signals. Scale bars, 50 μm. (**I**) IAHCs on the dorsal and ventral sides of the entire length of aorta counted separately and compared between control and NaOX-treated embryos. (**J**) Total number of cluster cells emerged on the dorsal and ventral sides of embryonic aorta compared between control and NaOX-treated embryos. (**K**) Size analysis of the IAHCs appeared in the aortic lumen in control and NaOX-treated embryos. Numbers of cells per cluster appeared in the embryonic aorta, each dot representing one cluster. (**L** to **P**) The proportion of (L) 1-cell, (M) 2- to 5-cell, (N) 6- to 10-cell, (O) 11- to 15-cell, and (P) 16-cell or larger clusters was plotted for control and NaOX-treated embryos. Data from 4 to 12 biological replicates are presented. Bars represent the means ± SEM. ns indicates $P > 0.05$; *$P < 0.05$, **$P < 0.01$, and ***$P < 0.001$ by two-tailed unpaired *t* test.

state (*29*). Therefore, we tested whether the treatment with NaOX led to any change in the oxidative means of energy production at the expense of glycolytic processes. We performed oxygen consumption rate (OCR) analysis on the sorted EC and HC populations of dissected AGM tissues from control and NaOX-treated embryos (Fig. 4, D to G). The endothelial fraction of the cells showed increase in the OCR (Fig. 4D), reflected in an increased ATP production (Fig. 4E). Although we did not observe any change in the glycolytic rate in hematopoietic fraction, we noted a robust increase in the basal aerobic respiration (Fig. 4, F and G). Increased mitochondrial metabolic activity was also reflected in an increased maximal respiration (fig. S5E) and ATP production (fig. S5F) in the hematopoietic

fraction. Overall, we concluded that NaOX treatment of the pregnant dams alters the metabolic state of the developing embryos, inhibiting aerobic glycolytic flux and inducing higher oxidative means of energy production. We used this model to understand the relevance of metabolic switch from a glycolytic to oxidative mode observed as the ECs transitioned into hematopoietic lineage. We performed IAHC analysis using whole-embryo immunostaining (Fig. 4H). The IAHCs were counted along the entire length of aorta divided into ventral and dorsal side (schematic in fig. S5G). The results showed that NaOX treatment led to a significant decrease in the number of IAHCs on both dorsal and ventral sides of the aorta (Fig. 4I). This was also reflected in a significantly reduced numbers of total c-kit$^+$ cells within the aorta (Fig. 4J). The effect was strong enough to result in a significant reduction in the number of c-kit$^+$ cells per IAHC (Fig. 4K). Upon analysis of size distribution of the IAHCs, we noted that there was a decrease in the proportion of one-cell IAHCs (Fig. 1L) with a concomitant increase in the two- to five-cell clusters (Fig. 4M). The relative proportion of clusters with more than five c-kit$^+$ cells remained unchanged (Fig. 4, N to P). These results indicate that there might be a stage-specific effect of metabolic change with a more robust impact on initial hematopoietic commitment.

As RUNX1 could further resolve IAHC heterogeneity and cellular composition within, we performed whole-mount immunostaining of embryos for RUNX1 along with CD31 and c-kit (Fig. 5, A and A′). Embryos with NaOX treatment showed a significant decrease in the number of RUNX1$^+$ IAHC cells in comparison to the embryos from untreated dams (Fig. 5B). Further analysis showed a similar decrease in the number of CD31$^+$RUNX1$^+$c-kit$^{+/high}$ IAHC cells in the DA (Fig. 5C). These results strongly suggested the importance of the glycolytic state of ECs in hematopoietic emergence in embryonic aorta. In addition to aorta, hematopoietic progenitors also emerge in other large arteries such as vitelline and umbilical arteries (UA) (*30*). To further support our data, we enquired whether the metabolic regulation of EHT and ensuing hematopoietic emergence follows same principle across hematopoietic sites. We analyzed the number of IAHCs in UA after NaOX treatment using whole-mount immunofluorescence imaging of control and NaOX-treated embryos (Fig. 5D). The results showed that NaOX treatment led to a significant decrease in the density of IAHCs in UA (presented as IAHCs/500 μm of the UA length; Fig. 5E).

We continued to explore the effect of inhibition of glycolytic flux using and performed explant cultures of the caudal part (CP) of the mid-gestation mouse embryos. The tissues were maintained ex vivo in the presence of stem cell factor (SCF), interleukin-3 (IL-3), and fms-like tyrosine kinase-3 ligand (FLT3L) for a period of 7 days, followed by methylcellulose-based colony-forming unit cell (CFU-C) assays to examine the function of the emerging hematopoietic system (schematic in fig. S6A). Results showed a clear decrease in the emergence of hematopoietic progenitors in the presence of NaOX, as there was a reduction of total CFU-C counts (Fig. 5F). Detailed analysis of individual colonies showed a specific decrease in the CFU-GM (granulocyte and macrophage) and the most primitive CFU-GEMM (granulocyte, erythrocyte, macrophage and megakaryocyte) colonies (Fig. 5G). We did not observe any change in the number of BFU-E (burst-forming unit-erythroid), CFU-G (granulocyte), and CFU-M (megakaryocyte) (Fig. 5G). These experiments were also performed using E9.5 embryos that showed similar results with reduced number of total CFU-Cs (fig. S6B). Among different progenitors, we noted a significant decrease in the numbers of BFU-E (fig. S6C). While no change was noted in CFU-G (fig. S6D) and CFU-M (fig. S6E), we observed a significant and robust decrease in the number of CFU-GM (fig. S6F) and CFU-GEMM (fig. S6G). To check the effect of direct inhibition of glycolysis in the process of EHT, we used 2-deoxy-D-glucose (2-DG; Fig. 5, H and I), a glucose analog that inhibits glycolysis via its actions on hexokinase, and PFK-015 (Fig. 5, J and K), a potent and selective 6-phosphofructo-2-kinase inhibitor. We performed explant culture of E10.5 CP with or without the presence of these inhibitors followed by colony formation assay. Results showed a clear decrease in the emergence of hematopoietic progenitors as reflected in the reduction of total CFU-C counts in 2-DG–treated embryo explants (Fig. 5H). Detailed analysis of individual colonies showed a decrease in the CFU-G, CFU-GM, and CFU-GEMM colonies (Fig. 5I). We did not observe any change in the number of BFU-E and CFU-M (Fig. 5I). Similarly, PFK-015 treatment also showed a significant reduction in total CFU-C counts (Fig. 5J) with a specific decrease in the CFU-G, CFU-M, CFU-GM, and CFU-GEMM colonies (Fig. 5K). These results showed that glycolytic function was crucial for EHT process. Enhancement in oxidative metabolic pathways inhibited the process of trans-differentiation of ECs into hematopoietic lineage in the mid-gestation mouse embryos.

Endothelial specific deletion of *Ldha* abrogates hematopoietic emergence

Pharmacologic inhibition of LDHA that induced an increase in the oxidative means with decreased glycolytic flux led to decreased hematopoietic emergence. These experiments targeted metabolic state systemically with possible indirect effects on the processes involved in EHT as well as off-target effects of pharmacologic intervention. To circumvent these issues, we used a genetic model wherein *Ldha* was deleted in hemato-ECs. *Tie2-Cre* and *Ldha*$^{fl/fl}$ mice were crossed (Fig. 6, A and B) to achieve biallelic deletion of *Ldha* (*Tie2-Ldha*$^{-/-}$), which were then used to examine the emergence of IAHCs in comparison to littermate controls (*Tie2-Ldha*$^{+/+}$ embryos). We performed whole-mount immunostaining of *Tie2-Ldha*$^{+/+}$ and *Tie2-Ldha*$^{-/-}$ embryos to analyze IAHCs within the DA (Fig. 6C). Quantification of emerging IAHCs on the dorsal and ventral sides of the dorsal aorta showed a clear decrease in the clusters per aorta in in *Tie2-Ldha*$^{-/-}$ embryos (Fig. 6D). The change in the number and distribution pattern of IAHCs in *Tie2-Ldha*$^{-/-}$ embryos were similar to what was observed in NaOX-treated embryos. We also noted a similar decrease in the total number of aortic cluster cells in aortic lumen, upon *Tie2-Cre*–mediated *Ldha* deletion (Fig. 6E). However, the reduction in the number of HCs was more robust on the ventral side. These results showed an overall decrease in the clusters size, as a decrease in the frequency of c-kit$^+$ cells per IAHC was observed (Fig. 6F). To rule out that these observations could be due to altered expression of c-kit, we performed quantification of its expression in IAHC cells. We analyzed the whole-mount immunostained *Tie2-Ldha*$^{+/+}$ and *Tie2-Ldha*$^{-/-}$ embryos and compared the MFI of signals for c-kit expression (fig. S7A). We did not observe any change in the intensity of c-kit signals in IAHC cells upon *Ldha* deletion (fig. S7B). Next, we performed size distribution for IAHCs in the aortic lumen, and we did not observe any change in the frequency of clusters based on their size (Fig. 6G). These results suggested uniform decrease in the cluster numbers irrespective of the size. Overall, these experiments confirmed the observations made via pharmacologic disruption of

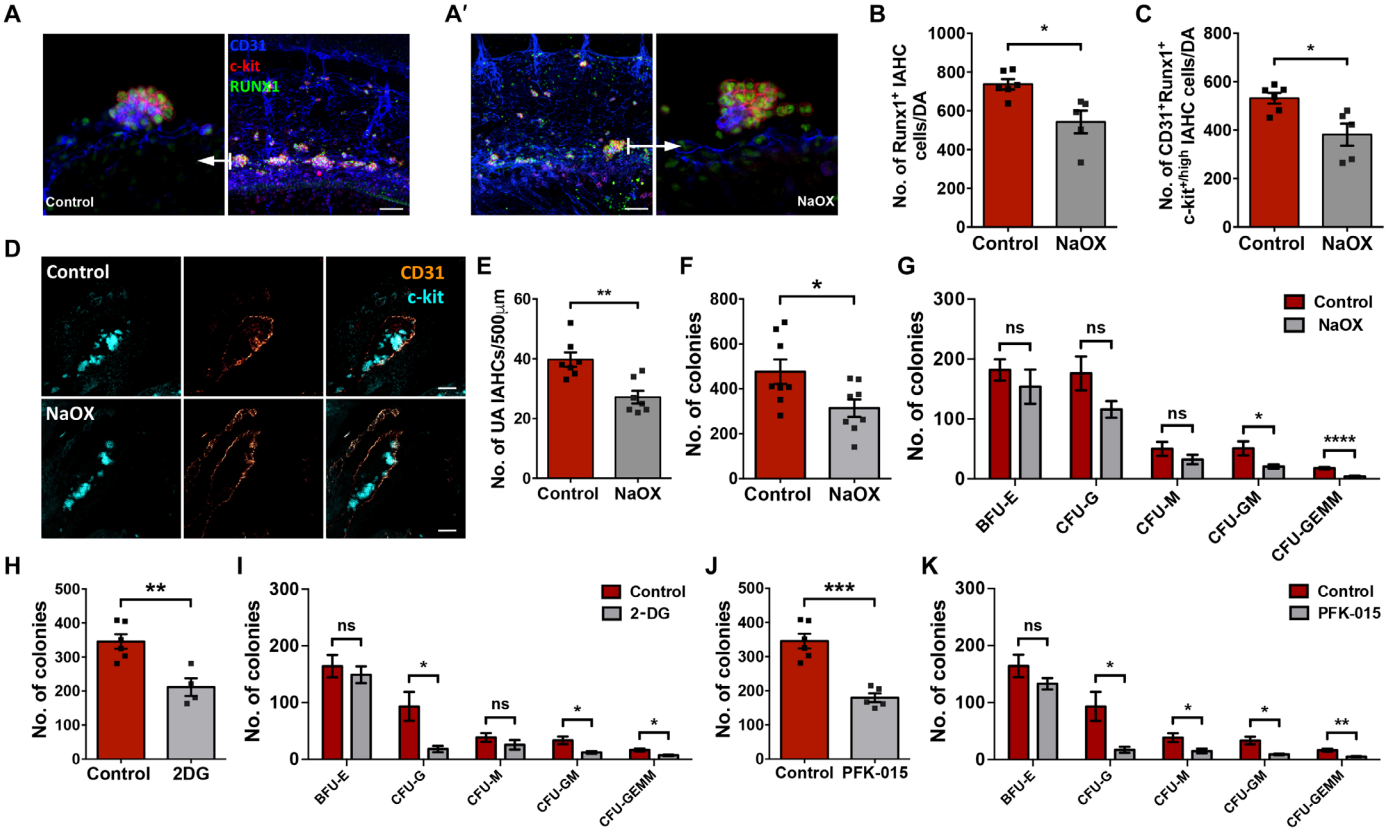

Fig. 5. Direct inhibition of glycolytic pathway reduces the emergence of hematopoietic progenitors in aorta. (**A** and **A**′) Whole-mount immunofluorescence imaging for IAHC analysis based on the expression of RUNX1 along with c-kit and CD31. Cluster analysis was performed for control (A) and NaOX-treated (A′) embryos. Scale bars, 50 μm. (**B**) Comparison of total number of RUNX1$^+$ cells in the aortic lumen in control and NaOX-treated embryos. (**C**) Number of CD31$^+$RUNX1$^+$c-kit$^{+/high}$ IAHC cells in the DA compared between control and NaOX-treated embryos. (**D**) Confocal-based immunofluorescence images of umbilical artery (UA) in control and NaOX-treated embryos immunostained with anti-CD31 and anti–c-kit antibodies. Scale bars, 50 μm. (**E**) Comparison of hematopoietic cluster density (IAHCs/500 μm of UA length) in UA of control and NaOX-treated embryos. (**F**) Comparison of the total colonies appeared in the explant cultures of E10.5 embryos maintained with or without NaOX for 7 days. (**G**) Number of different types of colonies, namely, BFU-Es, CFU-Gs, CFU-Ms, CFU-GMs, and CFU-GEMMs, obtained per cultured embryo explant. (**H** to **K**) Effect of direct inhibition of glycolysis on hematopoietic progenitor emergence. Ex vivo explant culture of mid-gestation embryonic caudal parts (CPs) was performed with or without the presence of 2-DG or PFK-015 followed by colony assay. (H) Comparison of the total number of colonies appeared in the explant cultures with or without 2-DG. (I) Number of different types of colonies appeared in CFU assay performed after the explant cultures with or without 2-DG. (J) Total number of colonies compared between embryo explants maintained with and without PF-015. (K) Comparison of different types of colonies obtained per embryo explant plotted for the two groups. Presented data are based on five to eight biological replicates. Bars represent the means ± SEM. ns indicates $P > 0.05$; *$P < 0.05$, **$P < 0.01$, ***$P < 0.001$, and ****$P < 0.0001$ by two-tailed unpaired *t* test.

LDHA activity. As observed following systemic inhibition of LDHA activity, *Tie2-Cre*–mediated deletion of *Ldha* led to a significant decrease in hematopoietic emergence in mid-gestation embryos.

Increased glycolytic flux mediated by VHL inhibition increases hematopoietic emergence

Our results established a metabolic shift from the glycolytic to oxidative state during the course of hematopoietic transition from endothelial lineage. Inhibition of glycolytic processes, achieved through pharmacological inhibition and *Tie2-Cre*–mediated deletion of *Ldha*, established the importance of the glycolytic state as they led to a decline in the hematopoietic emergence. In the next experiments, we aimed at stabilizing glycolytic process at the expense of mitochondrial function. Hypoxia pathway in response to cellular oxygen–sensing mechanism regulates the switch between glycolytic and mitochondrial metabolic states. We aimed to stabilize HIF-1α to inhibit mitochondrial function and increase glycolytic flux by using VHL inhibitor VH298. First, we examined the efficiency of VH298 to stabilize HIF-1α by performing whole-mount immunostaining of embryos from control and VH298-treated dams with HIF-1α antibody along with CD31 and c-kit. The results clearly showed higher levels of HIF-1α protein in IAHCs and vascular endothelium of VH298-treated embryos (fig. S8A). After confirming the efficacy of VH298 to stabilize HIF-1α, we performed metabolic flux analysis on the ECs and HCs sorted from AGM tissues dissected from embryos from control and VH298-treated pregnant dams (Fig. 7, A to D). We noted a robust decrease in OCR in ECs (Fig. 7, A to C) and HCs (Fig. 7D) from AGM. This showed a clear decrease in the mitochondrial respiration, confirming the effects of VHL inhibition in augmenting glycolytic flux at the expense oxidative metabolism. We followed this with the analysis of IAHCs following

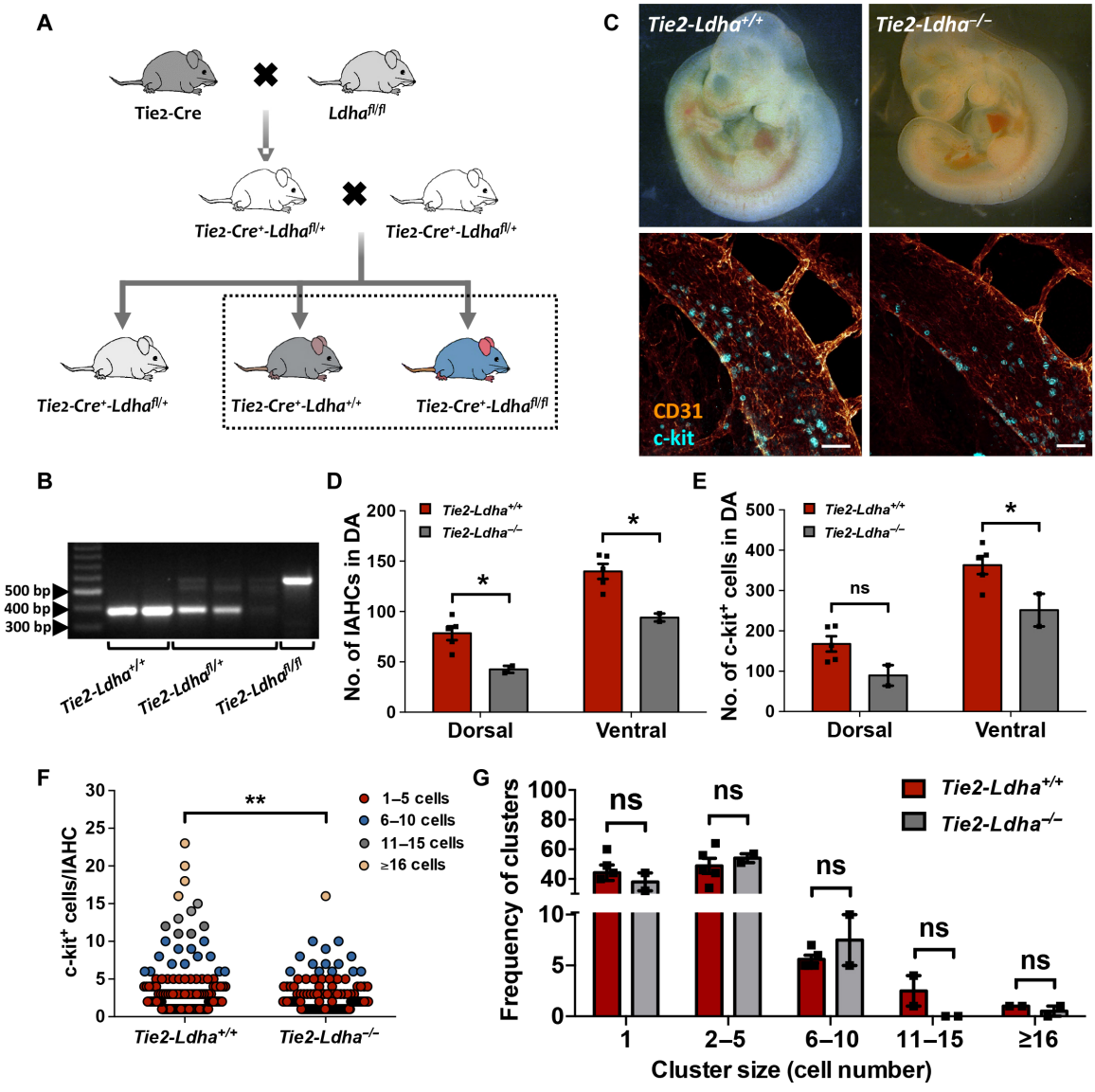

Fig. 6. LDHA deletion impairs HC emergence from aortic endothelium. (**A**) Schematic representation of breeding scheme used to generate *Tie2-Ldha*$^{+/+}$ and *Tie2-Ldha*$^{-/-}$ embryos. (**B**) PCR-based genotyping of the embryos using DNA extracted from tissues of E10.5 embryo proper. bp, base pairs. (**C**) Representative images showing gross morphology of the E10.5 *Tie2-Ldha*$^{+/+}$ and *Tie2-Ldha*$^{-/-}$ embryos in the top panel. Bottom panel shows whole-mount confocal images for the quantification of IAHCs in embryonic aorta. Maximum intensity projection images are shown with immunostaining performed for CD31 and c-kit on E10.5-genotyped embryos. Scale bars, 50 μm. (**D**) On the basis of the three-dimensional images obtained, we quantified the IAHCs on the dorsal and ventral sides across the aortic length. The numbers of IAHCs per aorta were compared between *Tie2-Ldha*$^{+/+}$ and *Tie2-Ldha*$^{-/-}$ embryos. (**E**) The number of cells in each hematopoietic cluster emerged from the aortic endothelium was counted. The total number of aortic cluster cells was compared between *Tie2-Ldha*$^{+/+}$ and *Tie2-Ldha*$^{-/-}$ embryos at E10.5. The total number of cluster cells appeared per embryo was plotted. (**F**) Comparison of cluster size between *Tie2-Ldha*$^{+/+}$ and *Tie2-Ldha*$^{-/-}$ embryos. The number of cells in each aortic cluster across the length of E10.5 embryo was plotted, each dot representing one IAHC. (**G**) Frequency distribution of differently sized clusters in embryonic aorta compared between *Tie2-Ldha*$^{+/+}$ and *Tie2-Ldha*$^{-/-}$ embryos. The proportion of clusters grouped according to the cell number per IAHC (1 cells, 2 to 5 cells, 6 to 10 cells, 11 to 15 cells, and 16 cells or larger) was plotted for each embryo. Presented data are based on two to five biological replicates. Data are represented as means ± SEM. ns indicates $P > 0.05$; *$P < 0.05$ and **$P < 0.01$ by two-tailed unpaired *t* test.

VH298 treatment for 24 hours (Fig. 7E). The results showed a clear increase in the emergence of hematopoietic clusters following VH298 treatment (Fig. 7F). This was in sharp contrast to the observations made following LDHA inhibition or deletion. IAHCs on the dorsal and ventral sides of the aortic lumen showed a significant increase upon VH298 treatment. We also noted an increase in the overall number of c-kit$^+$ cells emerged in the aorta after VH298 treatment (Fig. 7G). This increase in c-kit$^+$ cells was significant only for the clusters that appeared on the dorsal side of the aorta (Fig. 7H). However, it did result in an increase in the size of hematopoietic clusters as the number of c-kit$^+$ cells per cluster was significantly higher following VH298 treatment (Fig. 7I). However, the proportion of differently sized clusters did not show any change, reflecting a homogenous effect

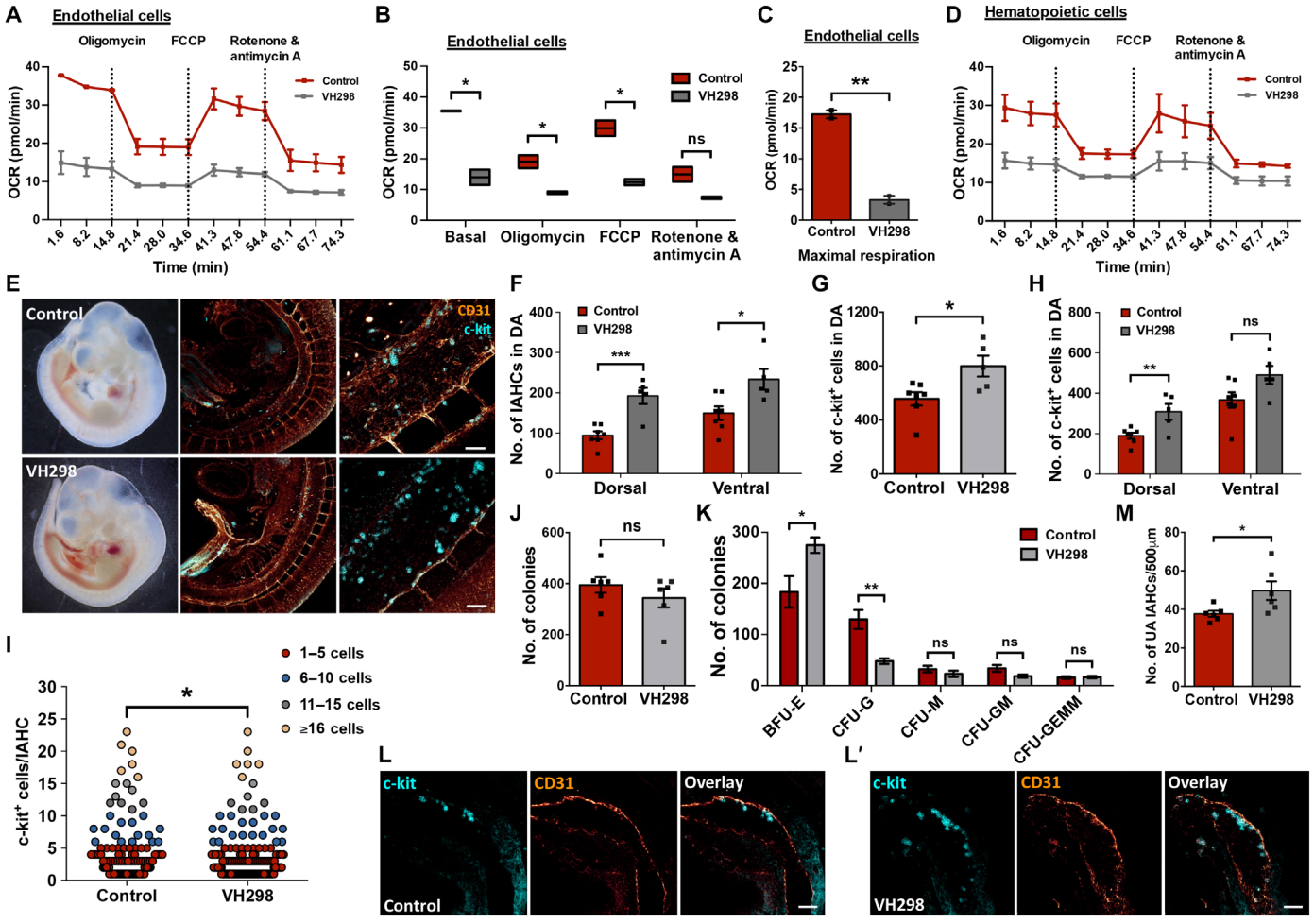

Fig. 7. Stabilization of HIF-1α promotes IAHC formation. (**A**) Mito stress test performed to examine the effect of VH298 on metabolic state of the aortic ECs. (**B**) Comparison of average OCR values in sorted aortic ECs before and after the addition of mitochondrial activity modulators. (**C**) Comparison of maximal respiration calculated from mito stress test. (**D**) Comparison of OCR examined by mito stress test performed using HCs sorted from control and VH298-treated E10.5 embryos. (**E**) Confocal microscopy–based whole-mount embryo imaging to compare the emergence of IAHCs in control and VH298-treated embryos ($n = 5$ to 8 independent biological replicates). The left panel shows gross morphology of the embryos imaged on a stereozoom microscope. The middle and right panels show confocal images for embryos immunostained for CD31 and c-kit. Scale bars, 50 μm. (**F**) Aortic clusters and (**G**) the total number of cluster cells counted for the dorsal and ventral sides along the aorta and compared between control and VH298-treated embryos. (**H**) Number of c-kit$^+$ cells in the aortic clusters along the dorsal and ventral side of DA in control and VH298-treated embryos. (**I**) Comparison between the control and VH298-treated embryos for c-kit$^+$ cells per cluster. (**J**) Comparison of the colonies appeared in the explant cultures of E10.5 embryos maintained with or without VH298. (**K**) Number of BFU-Es, CFU-Gs, CFU-Ms, CFU-GMs, and CFU-GEMMs obtained per cultured embryo explant plotted for the two groups. (**L**) Confocal-based whole-mount immunofluorescence images of UA in control and (**L′**) VH298-treated embryos stained for CD31 and c-kit. Scale bars, 50 μm. (**M**) Density of hematopoietic clusters represented as numbers normalized for a length of 500 μm of UA in control and NaOX-treated embryos. Data are represented as means ± SEM. ns indicates $P > 0.05$; *$P < 0.05$, **$P < 0.01$, and ***$P < 0.001$ by two-tailed unpaired t test.

(fig. S8B). In support of these results, we conducted explant culture of the CP of the mid-gestation embryos. The cultures were maintained for 7 days in the presence of SCF, Flt-3 L, and IL-3, with or without VH298 as performed for NaOX (schematic in fig. S6A). This was followed by comparison of emergence of hematopoietic progenitors in aortic tissues by performing methylcellulose colony assays. While we did not observe any significant change in the total number of colonies emerged after 7 days (Fig. 7J), we did observe an increase in the number of BFU-E colonies in cultures with VH298 (Fig. 7K). Direct impact of stabilization of hypoxic pathway on erythroid lineage differentiation might be the underlying reason, as we noted a decrease in the number of CFU-G colonies. There were comparable numbers of CFU-Gs, CFU-Ms, and CFU-GEMMs generated in both control and VH298-treated explants (Fig. 7K). We then went on test whether the effect of HIF-1α to stabilization was consistent for hematopoietic emergence in UA as well. As performed in the case of LDHA inhibition, hematopoietic clusters were enumerated and normalized for a length of 500 μm of UA of control (Fig. 7L) and VH298-treated (Fig. 7L′) embryos. The results showed a significant increase in the density of IAHCs that appeared in the UA of VH298-treated embryos in comparison to that of the control embryos (Fig. 7M). Hence, inhibition of oxygen-sensing pathway that results in the stabilization of HIF-1α led to an increase in the hematopoietic emergence. We concluded that a glycolytic state was crucial for the conversion of ECs to hematopoietic lineage.

DISCUSSION

BM-resident adult HSCs rely on glycolytic means of energy production and show very little mitochondrial activity (*31*). Mediated by ROS accumulation, induction of oxidative metabolic activity leads to functional decline (*32*). Contrarily, clearance of oxidative stress in freshly isolated mouse and human HSCs leads to improved hematopoietic recovery and function (*33*). As the master regulator of hypoxia response, HIF-1α plays a crucial role in determining the metabolic state of the cells. It was demonstrated that the level of HIF-1α stabilization fine-tunes the function of adult HSCs (*21*). Some of the transcriptional targets of HIF-1α are determinants of metabolic pathways and have been shown to regulate cell fate decisions in HSCs (*17*). With significant deviation in their function from the adult HSCs, embryonic and fetal HSCs present a specific case study in hematopoiesis. EHT is a unique trans-differentiation process that happens during embryonic development, leading to the emergence of a completely divergent cell type (*34*). In this process as well, hypoxia pathway was indicated to play an important role as in Zebrafish. The expression of *runx1* and *cmyb*, which are important determinants of hematopoietic emergence in aorta, is positively regulated by HIF-1α (*35*). These findings were confirmed using a mouse model wherein EC-specific deletion of *Hif-1α* resulted in a decrease in the hematopoietic emergence, demonstrated through in vitro hematopoietic progenitor assays (*22*). In addition, a significant decrease in the number of IAHCs and HECs was reported. Later, studies on Zebrafish hematopoietic emergence, it was elucidated that *Hif-2α* plays an additive role and a double deletion led to a more robust decrease in the hematopoietic emergence (*36*). A recent report showed that initiation of heartbeat provided triggered a metabolic switch essential for the process of EHT (*26*). Differential gene expression analysis indicated a decrease in the glycolytic processes during normal EHT process. However, description of the involvement of metabolic pathways in the process of hematopoietic emergence remained elusive.

We conducted a detailed analysis of the metabolic state of the cells during the process of EHT. Our proteomics data supported the involvement of a metabolic switch from glycolytic to oxidative respiration when the cells transited from endothelial to hematopoietic fate. Proteins associated with complex I biogenesis and respiratory electron transport processes were enriched in sorted HCs. Hypoxic response plays a very important role in deciding the metabolic pathways used by the cells to meet energy requirement. Stabilization of HIF-1α can directly lead to promotion of glycolytic pathways and inhibition of the flux toward oxidative phosphorylation (*37*). Although we did not observe up-regulation of glycolytic processes per se, several determinants were seen to be up-regulated in ECs. An increase in the level of mitochondrial activity upon hematopoietic transition also pointed toward this metabolic switch. Intriguingly, the total mitochondrial content remained higher in ECs, albeit with lower activity. Increased production of mitochondrial ROS confirmed an overall higher state of mitochondrial function.

Energy production via glycolytic pathways is less efficient and requires a higher level of glucose uptake that can support energy production. Higher glucose levels have been shown to suffice for a transition to induce expression of glycolytic enzymes and transition into an aerobic glycolytic state (*38*). Glucose uptake in a cell is governed by the level of expression of glucose transporters. As the kinetics of glucose transport varies across the transporter proteins, expression of specific glucose transporter may also affect glucose uptake (*39*). Increase in the glucose uptake was shown to induce *Hif-1α* expression stimulating hematopoietic development in Zebrafish aorta (*35*). We noted a significantly higher level of GLUT1 and GLUT3 expression, which is known to have highest turnover rate for glucose transport across the membrane. The differential level of GLUT1 and GLUT3 in ECs was reflected in an overall increase in the glucose uptake. It is also important to note that some of the enzymes involved in gluconeogenesis and galactose metabolism that can act as additional sources of glucose were also elevated in ECs. These experiments showed that metabolic machinery of the ECs supported glycolytic processes rather than mitochondrial respiration for energy production. Confirmation of the existence of a metabolic switch during the transition of endothelial to hematopoietic lineage came from extracellular flux analysis. Reflected in the ECAR, the ECs were clearly more glycolytic in their metabolic state that showed a robust decline upon trans-differentiation into hematopoietic lineage. These were rather unexpected findings and warranted exploration of the importance of the metabolic state in hematopoietic lineage commitment.

The metabolic state of the innate and adaptive immune cells has been shown to regulate their functional attributes (*40*). In the case of stem cells, the choice of metabolic pathways used has been linked to cell fate decisions (*41*). While the primitive HSCs were shown to remain in glycolytic state, their more differentiated progeny utilized mitochondrial pathways for energy production (*21*). A functional loss in HSCs due to genetic perturbations or physiological changes such as aging also involves metabolic shift to mitochondrial pathways (*42*). Therefore, it was intriguing to see the activation of mitochondrial pathways in the cells that acquired hematopoietic lineage. However, intrinsically, the aortic hematopoietic progenitors differ significantly from adult BM HSCs. As such, these hematopoietic progenitors are incapable of engrafting the adult hematopoietic system without ex vivo maturation (*3*). While they undergo a massive expansion and maturation in the FL and are easily engraftable in the adult BM, they still show that a significant transcriptomic difference remains distinct from adult HSCs (*43*). Our earlier data detected metabolic differences between the HSCs derived from FL and adult BM, wherein FL HSCs showed a remarkable up-regulation of mitochondrial function and oxidative metabolic pathways (*23*). This metabolic change also coincides with a major functional change in the HSCs, as they transition from a proliferative to a largely quiescent state (*44*).

Abrogation of oxygen-sensing pathway that resulted in enhanced glycolytic flux at the expense of oxidative processes, positively affected hematopoietic emergence. Both EC and HC populations showed a robust decrease in the OCR, following treatment with VHL inhibitor VH298 that stabilizes hypoxia pathway. A significant enhancement in the number of emerging clusters without any change in the proportion of differently sized IAHCs pointed to inhibition of early steps of hematopoietic commitment of the endothelial precursors. A recent study demonstrated the importance of Meis1, a transcription regulator of HIF-1α in the specification of hemogenic endothelium (*45*). This study very elegantly showed that Meis1 was responsible for early marking of ECs for hematopoietic commitment. These results could also point to the involvement of an intrinsically regulated HIF-1α pathway in EHT process that makes oxygenation status of the aorta less relevant to the overall process. On the contrary, mechanical forces exerted by the blood flow could play a bigger role in the induction of this process as

shown in Zebrafish (*46*). Biomechanical forces linked with the blood flow were implicated in the process of hematopoietic lineage commitment in vascular ECs both in vitro and in vivo (*47*, *48*).

Contrary to the impact on the IAHC and hematopoietic progenitor numbers, the explant cultures followed by methylcellulose-based colony-forming assay–based quantification of hematopoietic emergence did not show any change following VH298 treatment. Activation of hypoxia pathway has been shown to directly affect erythropoietic activity in HSC population (*49*), erythropoietin being the transcriptional target of HIF-1α (*50*). We did observe an increased output of BFU-E colonies in the explant cultures treated with VH298. As there was a corresponding decrease in the number of CFU-Gs, the total number of hematopoietic progenitors remained unchanged after 7 days of explant culture. Hence, the results from gain-of-function studies for the role of glycolytic state using stabilization of hypoxia pathway showed enhanced hematopoietic emergence. These findings complement earlier published loss-of-function studies for the role of HIF-1α.

Stabilization of hypoxia pathway also decreased mitochondrial function reflected in oxygen consumption rate. Increased hematopoietic emergence indicated that the oxidative metabolic state of the hematopoietic progenitors might not be crucial for overall development of the hematopoietic system. Results from experiments conducted using inhibition of LDHA by NaOX that resulted in gain of function for oxidative pathways at the expense of glycolytic processes were in congruence. In response to NaOX treatment, both endothelial and hematopoietic fractions of the dissected AGM-derived cells showed a robust increase in cellular OCR, indicative of elevated mitochondrial pathways. This led to clear inhibition of hematopoietic emergence in aorta reflected in the number of IAHCs that appeared in the dorsal and ventral sides. A robust decrease in the size of hematopoietic clusters showed that an increase in the mitochondrial function was important for the events after transition of endothelial to hematopoietic lineage. However, IAHC size distribution presented an interesting phenotype wherein a decrease in the single-cell clusters was noted with a similar increase in the bigger clusters. While these results pointed to an early-stage–specific role of glycolytic pathways, cell-specific deletion of *Ldha* in hemato-endothelial lineage did not follow this trend. It could also be concluded that, despite hematopoietic progenitors showing a higher level of mitochondrial metabolic pathway, an increase in the oxidative processes proved detrimental for overall hematopoietic emergence. Explant cultures of the CP of mid-gestation period embryos confirmed the results from IAHC analysis. The number of hematopoietic progenitors, reflected in the total number of CFU-Cs, decreased significantly in NaOX-treated explant cultures. Similar effects were noticed when glycolysis process was blocked using glucose analog 2-DG and PFK inhibitor PFK-015. While oxidative pathways can be compensated by alternative biochemical sources, these results show that glycolytic process cannot be compromised with, for a normal hematopoietic development. Hence, an increase in the oxidative metabolic pathways or a mere inhibition of anaerobic glycolytic process was sufficient for the abrogation of hematopoietic development. Tie2-Cre–mediated cell-specific deletion of *Ldha* was sufficient to mimic these effects almost entirely. *Tie2-Ldha*$^{-/-}$ embryos showed a strong inhibition of hematopoietic emergence at E10.5, similar to the observations made following NaOX treatment. These results indicated cell-intrinsic pathways affecting cell fate decisions in response to altered metabolic state. Again, we noted a sharp decline in c-kit^{+} cells per cluster, uniformly across clusters of different sizes, suggesting that oxidative pathways remain inhibitory even after hematopoietic commitment.

In conclusion, this study provides the first direct evidence of a metabolic switch that governs the EHT process in vertebrates. The glycolytic state of the ECs plays a crucial role in this trans-differentiation into hematopoietic lineage. Considering that the emergence of HSCs in the embryo takes place in the lumen of aorta with ample blood supply, how cell-intrinsic pathways use hypoxic means remains to be understood. This study also elucidates a metabolic link between oxygen sensing and hematopoietic emergence and function in mouse embryo. It is to be examined whether the outcome of this study could be applicable to the ongoing efforts to produce fully "mature" hematopoietic progenitors from the pluripotent stem cells.

MATERIALS AND METHODS

Mice

Twelve- to 16-week-old *Tie2-Cre* (gift from M. Yanagisawa) and *Ldha*$^{fl/fl}$ (gift from D. Scadden) mice were maintained in the animal facility of KU Leuven. C57BL/6J-NCBS mice were maintained in the animal facility of Indian Institute of Science Education and Research Thiruvananthapuram (IISER TVM). During the experiments, mice were maintained in individually isolated cages, fed with autoclaved acidified water, and irradiated food (Safe Diet, France) ad libitum. All procedures involving the use of animals were approved by the Institutional Animal Ethics Committees of IISER TVM and KU Leuven. At IISER TVM, experiments were conducted following the guidelines of the Committee for the Purpose of Control and Supervision of Experiments on Animals, Government of India.

Genotyping

Tie2-Cre and Ldha$^{fl/fl}$ mice were mated to get *Tie2-Ldha*$^{fl/+}$ mice that were mated again to get embryos with *Tie2-Cre*–mediated biallelic deletion of *Ldha* exon 3. Genotyping was performed on DNA isolated from tail tip for adult mice and skin tissues of individual mid-gestation embryos using the strategy as described before (*20*, *51*). All primer sequences are provided in table S1.

Embryo generation and embryonic tissue isolation

Eight- to 12-week-old adult male and female mice were used for timed mating to generate mid-gestation embryos. Observation of vaginal plugs was considered as E0.5 of mouse development. Embryos along with YS were removed from the uterus of the mother. YS were carefully removed leaving the vitelline and UA intact. Precise staging of embryos was done on the basis of the day of isolation and the number of somite pairs (sp). Embryos were collected at E10.5 (between 32 and 36 sp) of development in phosphate-buffered saline (PBS) supplemented with 10% of fetal bovine serum (FBS).

Pharmacologic treatment of pregnant females

Pharmacologic inhibition of anaerobic glycolysis was achieved by intraperitoneal injection of E9.5 pregnant mice with LDHA inhibitor NaOX (300 mg/kg; Sigma-Aldrich). Stabilization of HIF-1α in the developing embryos was achieved by intraperitoneal injection of VHL inhibitor VH298 (150 mg/kg; Sigma-Aldrich). In both cases, embryos were harvested 24 hours (at E10.5) after treatment.

Flow cytometry and cell sorting

For analysis of the cells in different stages of EHT, cells obtained from dissected AGM tissues were immunolabeled with fluorophore-conjugated antibodies against specific markers. Dissected AGMs from the embryos were pooled, dissociated by 0.35% collagenase I (Sigma-Aldrich) (0.35% enzyme in PBS with 20% FBS) treatment for 30 min at 37°C, and washed with PBS containing 10% FBS. The dissociated AGM cells were stained with allophycocyanin/cyanine7–conjugated anti–c-kit (CD117) and phycoerythrin-conjugated anti-CD31 antibodies (from BioLegend) and sorted on a BD FACSAria III sorter using a 70-μm nozzle. EC, HEC, and HC populations were identified as $CD31^{+}$c-kit^{-}, $CD31^{+}$c-kit^{+}, and $CD31^{-}$c-kit^{+}, respectively. The cell populations were sorted by FACS, using a FACSAria III (Becton Dickinson). Details of clones used for each antibody are provided in the Supplementary Materials.

Mitochondrial mass, ROS, and glucose uptake analyses

Mitochondrial mass, active mitochondrial content, and mitochondrial ROS were assessed by MitoTracker Green FM, MitoSOX Red, and MitoTracker Red CMXRos staining, respectively. Briefly, following immunostaining for CD31 and c-kit, single-cell suspension of AGM was incubated with MitoTracker Green (150 nM), MitoSOX Red (10 μM), or MitoTracker Red CMXRos (100 nM) in PBS containing 5% FBS for 30 and 15 min, respectively, at 37°C. Glucose transporter expression was analyzed by staining single-cell suspension prepared from dissected AGM tissue with fluorescein isothiocyanate–conjugated anti-GLUT3 antibody or primary anti-GLUT1 antibody along with CD31 and c-kit antibodies for 20 min on ice. Immunostaining with purified primary antibody was followed by additional PBS wash and incubation with fluorophore-conjugated secondary antibodies. For glucose uptake assay, AGM cell suspension after CD31 and c-kit immune-staining was incubated with 2-NBDG (200 μM), a fluorescent glucose analog for 20 min at 37°C. After staining, the cells were washed with PBS and analyzed using a BD FACSAria III cytometer. The flow cytometry data including MFI was analyzed using FlowJo software (BD Biosciences) with isotype-stained/unlabeled cells as negative controls.

Sample preparation for proteome analysis

FACS-sorted ECs (c-$kit^{-}CD31^{+}$), HECs (c-$kit^{+}CD31^{+}$), HCs (c-$kit^{+}CD31^{-}$), and DNCs (c-$kit^{-}CD31^{-}$) from E10.5 AGM were suspended in 100 μl of lysis buffer [0.01 M tris base (pH7.4), 0.14 M NaCl, 1% Triton X-100, and 1 mM phenylmethylsulfonyl fluoride] prepared in LiChrosolv water for chromatography and sonicated for 15 min. To each 100 μl of cell lysate, 900 μl of ice-cold acetone was added, and, after incubation at −20°C for 20 min, lysates were centrifuged at 17,400 relative centrifugal force (rcf) for 10 min. Precipitate was dissolved in 250 μl of LC/MS grade water and reprecipitated using 900 μl of ice-cold acetone followed by centrifugation. Pelleted proteins were suspended in 100 μl of 50 mM ammonium bicarbonate and thermally denatured at 65°C for 10 min. Proteins were then reduced by adding 2.5 μl of 200 mM dithiothreitol (DTT) solution and incubation at 60°C for 45 min followed by alkylation with addition of 10 μl of iodoacetamide (IAA) and incubation at 37°C for 45 min. A second reduction by 2.5 μl of aliquot of 200 mM DTT was added and followed by incubation at 37°C for 30 min to consume excess IAA. Protein was then digested by the addition of 4 μg of SOLu-Trypsin and incubated at 37°C overnight. The enzymatic digestion was quenched by adding 1 μl of formic acid, and the samples were speed-vacuum–dried and resuspended in 100 μl of ammonium bicarbonate before desalting. Desalting was performed by PierceTM C-18 spin columns as per the manufacturer's protocol before analysis.

MS analysis

Before MS analysis, all samples were resuspended in 50 μl of 0.1% formic acid. Ten microliters of each sample (0.2 ± 0.05 mg/ml) in triplicates was analyzed on a Thermo Fisher Scientific EASY-nLC 1000 system directly connected to the Thermo Fisher Scientific The Q Exactive – A Benchtop Orbitrap Mass Spectrometer. Acclaim PepMap 100 C18 (3 μm, 75 μm by 20 mm; nanoViper Trap, 1200 bar; Thermo Fisher Scientific) trap column and Acclaim PepMap 100 C18 HPLC (2 μm, 75 μm by 150 mm; nanoViper FS, 1200 bar; Thermo Fisher Scientific) analytical column were used for the separation of sample. The mobile phases A and B consisted of 0.1% formic acid in LiChrosolv water for chromatography and LiChrosolv Reag. Ph Eur. acetonitrile, respectively. The applied 140-min multistep gradient ranged from 5 to 95% mobile phase B at a constant flow rate of 300 nl/min. The eluent was directly introduced into the mass spectrometer via Thermo Fisher Scientific Nanospray Flex ion source connected with the Thermo Fisher Scientific Nano Bore Emitter Stainless Steel of 40 mm with an outer diameter of 1/32 inch. The applied spray voltage was 18000.00 (+) and 2000.00 (−), and the capillary temperature was set to 250°C. We measured in positive ion mode. Full-scan MS spectra were recorded from 350 to 1500 mass/charge ratio at resolution 70,000 followed by MS/MS spectra recorded from 200 to 2000 scans at resolution 17,500. Protein identification and quantification were performed using Thermo Fisher Scientific Proteome Discoverer Software (version 2.3). Peptides with more than six amino acids were considered during the entire analysis. For proteome comparison between cell types of E10.5 AGM, values for the protein technical replicates ($N = 3$) were taken with the average of all detected values, and the biological replicates ($n = 3$) were imputed by taking the average of the nonzero values. Single-value imputation refers to replacing missing values by a constant or a randomly selected value. Here, we have replaced the blank values with the lowest abundance value detected. Differential proteome expression analysis was carried out using RStudio. Pathway enrichment analysis was performed with the Reactome Pathway Database by comparing proteome generated by MS for each cell type with UniProt2Reactome.txt and analyzed by RStudio.

Seahorse metabolic flux analysis

The glycolytic rate (ECAR) and the mitochondrial respiration rate (OCR) in cell populations from IAHCs, namely, ECs, HECs, and HCs were accessed using seahorse XFp-Analyzer (Agilent, USA) as described by the manufacturer. Briefly, cells pooled from AGM tissues were sorted on FACSAria III, and 30,000 cells were plated into each well of SeaHorse XFp cell culture miniplates pre-coated with Cell Tak (Corning). The plates were allowed to equilibrate in a non-CO_2 incubator at 37°C for 30 min before analysis. For ECAR analysis, XF base medium was supplemented with glutamine (0.584 g/liter). ECAR was measured in basal condition, and three readings were taken after sequential addition of glucose (10 mM), oligomycin (1 μM), and 2-DG (50 mM) into the injection ports. For OCR analysis, XF base medium was supplemented with glutamine (0.584 g/liter), glucose (4.5 g/liter), and 1 mM sodium pyruvate. OCR was measured in basal condition and after sequential addition of oligomycin (1 μM),

carbonyl cyanide *p*-trifluoromethoxyphenylhydrazone (2 μM), rotenone (0.5 μM), and antimycin A (0.5 μM) into the injection ports. Metabolic parameters were derived following the manufacturer's instructions (Agilent, USA).

Whole-mount immunofluorescence analysis

Embryos followed by sp. counting were stained for whole-mount immunofluorescence analysis as previously described (*9*). Briefly, the embryos were fixed in 2% paraformaldehyde in PBS, trimmed, and stained for CD31 and c-kit followed by Alexa Fluor–conjugated secondary antibodies. For GLUT1, RUNX1, and HIF-1α staining, an additional incubation with purified primary antibody followed by washing with PBS containing 0.1% skimmed milk and 0.4% Triton X-100. The embryos were then incubated with fluorophore-conjugated secondary antibodies before washing thrice in PBS-MT. Washed embryos were then dehydrated, cleared, and mounted with a 1:2 mix of benzyl alcohol and benzyl benzoate in FastWells incubation chamber (Grace Bio-Labs, USA). Image acquisition was performed using a Leica upright confocal microscope system using a 10× or a 40× water dipping objective. Image processing was carried out using LAS X software. For quantification of IAHCs, the entire length of aorta divided into ventral and dorsal side. Hematopoietic clusters were counted separately for the ventral and dorsal sides. In addition, the number of c-kit$^+$ cells were also enumerated for each cluster.

Explant culture and methylcellulose colony-forming assay

The explant culture of the tissues from mid-gestation stage embryos was performed as previously described with modifications (*52*). Briefly, the CP of the E10.5 embryos was dissected just above the forelimbs, and the FL and heart were removed and cultured for 7 days on top of 0.8-μm–pore size mixed cellulose membranes at the gas-liquid interface in Iscove's modified Dulbecco's medium supplemented with 20% FBS and IL-3 (100 ng/ml), SCF (100 ng/ml), and FLT3L (100 ng/ml) (all growth factors procured from R&D systems Inc.). The explants were maintained in the medium containing NaOX (500 mM), VH298 (10 μM), 2-DG (100 μM), PFK-015 (10 μM), or dimethyl sulfoxide as carrier control for 7 days. The tissues were then dissociated by collagenase treatment (0.35% collagenase type I in PBS with 20% FBS) for 30 min at 37°C. The cells were plated in tissue culture–treated six-well plates (CytoOne) in duplicate wells in MethoCult (STEMCELL Technologies) and cultured at 37°C, and colonies were scored after 7 days.

Quantitative reverse transcription PCR

AGM from mid-gestation mouse embryos were dissected, dissociated into single-cell suspensions, and subjected to FACS-based sorting of EC, HEC, and HC cell populations. Total RNA was isolated from each population using an RNeasy plus Micro kit (QIAGEN) and subjected to cDNA synthesis using a PrimeScript RT reagent kit (Takara). Real-time quantitative PCR was performed using the TB Green Premix (Takara) in a CFX96 Real-Time PCR system (Bio-Rad) following the standard protocols using primers in table S1. Relative gene expression was calculated by comparative cycle threshold (Ct) method and normalized to actin expression.

Statistical analysis and data visualization

Statistical analyses and data visualization were performed using GraphPad Prism and RStudio. The data with normal distribution, tested by using the Shapiro-Wilk test, are represented as means ± SEM. Data with non-normal distribution are represented in scatter plots. The equality of group variance was tested using Brown-Forsythe test. Comparisons between samples from two groups with normally distributed data with equal variance were made using the unpaired two-tailed Student's *t* test. Schematics and graphical abstract were generated in part by BioRender (www.biorender.com/). For all analyses, *P* value of ≤0.05 was accepted as statistically significant. Asterisks in the figures indicate statistical significance: $*P < 0.05$, $**P < 0.01$, $***P < 0.001$, and $****P < 0.0001$.

Supplementary Materials

This PDF file includes:

Figs. S1 to S8

Tables S1 to S3

REFERENCES AND NOTES

1. H. K. Mikkola, S. H. Orkin, The journey of developing hematopoietic stem cells. *Development* **133**, 3733–3744 (2006).
2. C. Boiers, J. Carrelha, M. Lutteropp, S. Luc, J. C. Green, E. Azzoni, P. S. Woll, A. J. Mead, A. Hultquist, G. Swiers, E. G. Perdiguero, I. C. Macaulay, L. Melchiori, T. C. Luis, S. Kharazi, T. Bouriez-Jones, Q. Deng, A. Ponten, D. Atkinson, C. T. Jensen, E. Sitnicka, F. Geissmann, I. Godin, R. Sandberg, M. F. de Bruijn, S. E. Jacobsen, Lymphomyeloid contribution of an immune-restricted progenitor emerging prior to definitive hematopoietic stem cells. *Cell Stem Cell* **13**, 535–548 (2013).
3. A. Medvinsky, E. Dzierzak, Definitive hematopoiesis is autonomously initiated by the AGM region. *Cell* **86**, 897–906 (1996).
4. S. Taoudi, A. Medvinsky, Functional identification of the hematopoietic stem cell niche in the ventral domain of the embryonic dorsal aorta. *Proc. Natl. Acad. Sci. U.S.A.* **104**, 9399–9403 (2007).
5. E. Dzierzak, A. Bigas, Blood development: Hematopoietic stem cell dependence and independence. *Cell Stem Cell* **22**, 639–651 (2018).
6. P. Gao, C. Chen, E. D. Howell, Y. Li, J. Tober, Y. Uzun, B. He, L. Gao, Q. Zhu, A. F. Siekmann, N. A. Speck, K. Tan, Transcriptional regulatory network controlling the ontogeny of hematopoietic stem cells. *Genes Dev.* **34**, 950–964 (2020).
7. K. Kissa, P. Herbomel, Blood stem cells emerge from aortic endothelium by a novel type of cell transition. *Nature* **464**, 112–115 (2010).
8. E. de Pater, P. Kaimakis, C. S. Vink, T. Yokomizo, T. Yamada-Inagawa, R. van der Linden, P. S. Kartalaei, S. A. Camper, N. Speck, E. Dzierzak, Gata2 is required for HSC generation and survival. *J. Exp. Med.* **210**, 2843–2850 (2013).
9. T. Yokomizo, C. E. Ng, M. Osato, E. Dzierzak, Three-dimensional imaging of whole midgestation murine embryos shows an intravascular localization for all hematopoietic clusters. *Blood* **117**, 6132–6134 (2011).
10. J. Tober, A. D. Yzaguirre, E. Piwarzyk, N. A. Speck, Distinct temporal requirements for Runx1 in hematopoietic progenitors and stem cells. *Development* **140**, 3765–3776 (2013).
11. M. J. Chen, T. Yokomizo, B. M. Zeigler, E. Dzierzak, N. A. Speck, Runx1 is required for the endothelial to haematopoietic cell transition but not thereafter. *Nature* **457**, 887–891 (2009).
12. N. C. Denko, Hypoxia, HIF1 and glucose metabolism in the solid tumour. *Nat. Rev. Cancer* **8**, 705–713 (2008).
13. P. Koivunen, T. Kietzmann, Hypoxia-inducible factor prolyl 4-hydroxylases and metabolism. *Trends Mol. Med.* **24**, 1021–1035 (2018).
14. G. L. Semenza, P. H. Roth, H. M. Fang, G. L. Wang, Transcriptional regulation of genes encoding glycolytic-enzymes by hypoxia-inducible factor-1. *J. Biol. Chem.* **269**, 23757–23763 (1994).
15. J. W. Kim, I. Tchernyshyov, G. L. Semenza, C. V. Dang, HIF-1-mediated expression of pyruvate dehydrogenase kinase: A metabolic switch required for cellular adaptation to hypoxia. *Cell Metab.* **3**, 177–185 (2006).
16. C. E. Forristal, I. G. Winkler, B. Nowlan, V. Barbier, G. Walkinshaw, J. P. Levesque, Pharmacologic stabilization of HIF-1α increases hematopoietic stem cell quiescence in vivo and accelerates blood recovery after severe irradiation. *Blood* **121**, 759–769 (2013).
17. K. Takubo, G. Nagamatsu, C. I. Kobayashi, A. Nakamura-Ishizu, H. Kobayashi, E. Ikeda, N. Goda, Y. Rahimi, R. S. Johnson, T. Soga, A. Hirao, M. Suematsu, T. Suda, Regulation of glycolysis by Pdk functions as a metabolic checkpoint for cell cycle quiescence in hematopoietic stem cells. *Cell Stem Cell* **12**, 49–61 (2013).
18. T. Simsek, F. Kocabas, J. Zheng, R. J. Deberardinis, A. I. Mahmoud, E. N. Olson, J. W. Schneider, C. C. Zhang, H. A. Sadek, The distinct metabolic profile of hematopoietic stem cells reflects their location in a hypoxic niche. *Cell Stem Cell* **7**, 380–390 (2010).
19. T. Suda, K. Takubo, G. L. Semenza, Metabolic regulation of hematopoietic stem cells in the hypoxic niche. *Cell Stem Cell* **9**, 298–310 (2011).

20. Y. H. Wang, W. J. Israelsen, D. Lee, V. W. C. Yu, N. T. Jeanson, C. B. Clish, L. C. Cantley, M. G. Vander Heiden, D. T. Scadden, Cell-state-specific metabolic dependency in hematopoiesis and leukemogenesis. *Cell* **158**, 1309–1323 (2014).
21. K. Takubo, N. Goda, W. Yamada, H. Iriuchishima, E. Ikeda, Y. Kubota, H. Shima, R. S. Johnson, A. Hirao, M. Suematsu, T. Suda, Regulation of the HIF-1alpha level is essential for hematopoietic stem cells. *Cell Stem Cell* **7**, 391–402 (2010).
22. P. Imanirad, P. Solaimani Kartalaei, M. Crisan, C. Vink, T. Yamada-Inagawa, E. de Pater, D. Kurek, P. Kaimakis, R. van der Linden, N. Speck, E. Dzierzak, HIF1α is a regulator of hematopoietic progenitor and stem cell development in hypoxic sites of the mouse embryo. *Stem Cell Res.* **12**, 24–35 (2014).
23. J. K. Manesia, Z. F. Xu, D. Broekaert, R. Boon, A. van Vliet, G. Eelen, T. Vanwelden, S. Stegen, N. Van Gastel, A. Pascual-Montano, S. M. Fendt, G. Carmeliet, P. Carmeliet, S. Khurana, C. M. Verfaillie, Highly proliferative primitive fetal liver hematopoietic stem cells are fueled by oxidative metabolic pathways. *Stem Cell Res.* **15**, 715–721 (2015).
24. K. Ito, A. Hirao, F. Arai, K. Takubo, S. Matsuoka, K. Miyamoto, M. Ohmura, K. Naka, K. Hosokawa, Y. Ikeda, T. Suda, Reactive oxygen species act through p38 MAPK to limit the lifespan of hematopoietic stem cells. *Nat. Med.* **12**, 446–451 (2006).
25. A. Biswas, I. M. Roy, P. C. Babu, J. Manesia, S. Schouteden, V. Vijayakurup, R. J. Anto, J. Huelsken, A. Lacy-Hulbert, C. M. Verfaillie, S. Khurana, The periostin/integrin-αV axis regulates the size of hematopoietic stem cell pool in the fetal liver. *Stem Cell Reports* **15**, 340–357 (2020).
26. E. Azzoni, V. Frontera, G. Anselmi, C. Rode, C. James, E. M. Deltcheva, A. S. Demian, J. Brown, C. Barone, A. Patelli, J. R. Harman, M. Nicholls, S. J. Conway, E. Morrissey, S. E. W. Jacobsen, D. B. Sparrow, A. L. Harris, T. Enver, M. de Bruijn, The onset of circulation triggers a metabolic switch required for endothelial to hematopoietic transition. *Cell Rep.* **37**, 110103 (2021).
27. K. C. Patra, N. Hay, The pentose phosphate pathway and cancer. *Trends Biochem. Sci.* **39**, 347–354 (2014).
28. J. Papaconstantinou, S. P. Colowick, The role of glycolysis in the growth of tumor cells. *J. Biol. Chem.* **236**, 285–288 (1961).
29. D. Hu, A. Linders, A. Yamak, C. Correia, J. D. Kijlstra, A. Garakani, L. Xiao, D. J. Milan, P. van der Meer, M. Serra, P. M. Alves, I. J. Domian, Metabolic maturation of human pluripotent stem cell-derived cardiomyocytes by inhibition of HIF1α and LDHA. *Circ. Res.* **123**, 1066–1079 (2018).
30. A. D. Yzaguirre, N. A. Speck, Insights into blood cell formation from hemogenic endothelium in lesser-known anatomic sites. *Dev. Dyn.* **245**, 1011–1028 (2016).
31. H. W. Snoeck, Mitochondrial regulation of hematopoietic stem cells. *Curr. Opin. Cell Biol.* **49**, 91–98 (2017).
32. I. M. Roy, A. Biswas, C. Verfaillie, S. Khurana, Energy producing metabolic pathways in functional regulation of the hematopoietic stem cells. *IUBMB Life* **70**, 612–624 (2018).
33. C. R. Mantel, H. A. O'Leary, B. R. Chitteti, X. Huang, S. Cooper, G. Hangoc, N. Brustovetsky, E. F. Srour, M. R. Lee, S. Messina-Graham, D. M. Haas, N. Falah, R. Kapur, L. M. Pelus, N. Bardeesy, J. Fitamant, M. Ivan, K. S. Kim, H. E. Broxmeyer, Enhancing hematopoietic stem cell transplantation efficacy by mitigating oxygen shock. *Cell* **161**, 1553–1565 (2015).
34. A. M. Muller, A. Medvinsky, J. Strouboulis, F. Grosveld, E. Dzierzak, Development of hematopoietic stem cell activity in the mouse embryo. *Immunity* **1**, 291–301 (1994).
35. J. M. Harris, V. Esain, G. M. Frechette, L. J. Harris, A. G. Cox, M. Cortes, M. K. Garnaas, K. J. Carroll, C. C. Cutting, T. Khan, P. M. Elks, S. A. Renshaw, B. C. Dickinson, C. J. Chang, M. P. Murphy, B. H. Paw, M. G. Vander Heiden, W. Goessling, T. E. North, Glucose metabolism impacts the spatiotemporal onset and magnitude of HSC induction in vivo. *Blood* **121**, 2483–2493 (2013).
36. C. Gerri, M. Marass, A. Rossi, D. Y. R. Stainier, Hif-1α and Hif-2α regulate hemogenic endothelium and hematopoietic stem cell formation in zebrafish. *Blood* **131**, 963–973 (2018).
37. S. J. Kierans, C. T. Taylor, Regulation of glycolysis by the hypoxia-inducible factor (HIF): Implications for cellular physiology. *J. Physiol.* **599**, 23–37 (2021).
38. E. F. Greiner, M. Guppy, K. Brand, Glucose is essential for proliferation and the glycolytic enzyme induction that provokes a transition to glycolytic energy production. *J. Biol. Chem.* **269**, 31484–31490 (1994).
39. K. Adekola, S. T. Rosen, M. Shanmugam, Glucose transporters in cancer metabolism. *Curr. Opin. Oncol.* **24**, 650–654 (2012).
40. K. Ganeshan, A. Chawla, Metabolic regulation of immune responses. *Annu. Rev. Immunol.* **32**, 609–634 (2014).
41. C. E. Meacham, A. W. DeVilbiss, S. J. Morrison, Metabolic regulation of somatic stem cells in vivo. *Nat. Rev. Mol. Cell Biol.* **23**, 428–443 (2022).
42. T. T. Ho, M. R. Warr, E. R. Adelman, O. M. Lansinger, J. Flach, E. V. Verovskaya, M. E. Figueroa, E. Passegué, Autophagy maintains the metabolism and function of young and old stem cells. *Nature* **543**, 205–210 (2017).
43. S. McKinney-Freeman, P. Cahan, H. Li, S. A. Lacadie, H. T. Huang, M. Curran, S. Loewer, O. Naveiras, K. L. Kathrein, M. Konantz, E. M. Langdon, C. Lengerke, L. I. Zon, J. J. Collins, G. Q. Daley, The transcriptional landscape of hematopoietic stem cell ontogeny. *Cell Stem Cell* **11**, 701–714 (2012).
44. M. B. Bowie, D. G. Kent, B. Dykstra, K. D. McKnight, L. McCaffrey, P. A. Hoodless, C. J. Eaves, Identification of a new intrinsically timed developmental checkpoint that reprograms key hematopoietic stem cell properties. *Proc. Natl. Acad. Sci. U.S.A.* **104**, 5878–5882 (2007).
45. P. Coulombe, G. Cole, A. Fentiman, J. D. K. Parker, E. Yung, M. Bilenky, L. Degefie, P. Lac, M. Y. M. Ling, D. Tam, R. K. Humphries, A. Karsan, Meis1 establishes the pre-hemogenic endothelial state prior to Runx1 expression. *Nat. Commun.* **14**, 4537 (2023).
46. T. E. North, W. Goessling, M. Peeters, P. Li, C. Ceol, A. M. Lord, G. J. Weber, J. Harris, C. C. Cutting, P. Huang, E. Dzierzak, L. I. Zon, Hematopoietic stem cell development is dependent on blood flow. *Cell* **137**, 736–748 (2009).
47. L. Adamo, O. Naveiras, P. L. Wenzel, S. McKinney-Freeman, P. J. Mack, J. Gracia-Sancho, A. Suchy-Dicey, M. Yoshimoto, M. W. Lensch, M. C. Yoder, G. Garcia-Cardena, G. Q. Daley, Biomechanical forces promote embryonic haematopoiesis. *Nature* **459**, 1131–1135 (2009).
48. M. F. Diaz, N. Li, H. J. Lee, L. Adamo, S. M. Evans, H. E. Willey, N. Arora, Y. S. Torisawa, D. A. Vickers, S. A. Morris, O. Naveiras, S. K. Murthy, D. E. Ingber, G. Q. Daley, G. Garcia-Cardena, P. L. Wenzel, Biomechanical forces promote blood development through prostaglandin E2 and the cAMP-PKA signaling axis. *J. Exp. Med.* **212**, 665–680 (2015).
49. H. M. Rogers, X. Yu, J. Wen, R. Smith, E. Fibach, C. T. Noguchi, Hypoxia alters progression of the erythroid program. *Exp. Hematol.* **36**, 17–27 (2008).
50. G. L. Semenza, G. L. Wang, A nuclear factor induced by hypoxia via de novo protein synthesis binds to the human erythropoietin gene enhancer at a site required for transcriptional activation. *Mol. Cell. Biol.* **12**, 5447–5454 (1992).
51. Y. Y. Kisanuki, R. E. Hammer, J. Miyazaki, S. C. Williams, J. A. Richardson, M. Yanagisawa, Tie2-Cre transgenic mice: A new model for endothelial cell-lineage analysis in vivo. *Dev. Biol.* **230**, 230–242 (2001).
52. S. Gordon-Keylock, M. Sobiesiak, S. Rybtsov, K. Moore, A. Medvinsky, Mouse extraembryonic arterial vessels harbor precursors capable of maturing into definitive HSCs. *Blood* **122**, 2338–2345 (2013).
53. E. W. Deutsch, A. Csordas, Z. Sun, A. Jarnuczak, Y. Perez-Riverol, T. Ternent, D. S. Campbell, M. Bernal-Llinares, S. Okuda, S. Kawano, R. L. Moritz, J. J. Carver, M. Wang, Y. Ishihama, N. Bandeira, H. Hermjakob, J. A. Vizcaino, The ProteomeXchange consortium in 2017: Supporting the cultural change in proteomics public data deposition. *Nucleic Acids Res.* **45**, D1100–D1106 (2017).
54. M. Choi, J. Carver, C. Chiva, M. Tzouros, T. Huang, T. H. Tsai, B. Pullman, O. M. Bernhardt, R. Huttenhain, G. C. Teo, Y. Perez-Riverol, J. Muntel, M. Muller, S. Goetze, M. Pavlou, E. Verschueren, B. Wollscheid, A. I. Nesvizhskii, L. Reiter, T. Dunkley, E. Sabido, N. Bandeira, O. Vitek, MassIVE.quant: A community resource of quantitative mass spectrometry-based proteomics datasets. *Nat. Methods* **17**, 981–984 (2020).

Acknowledgments: We acknowledge the support from Mass Spectrometry Unit of the Central Instrumentation Facility (CIF) at IISER Thiruvananthapuram for the proteomic analysis. We also thank Pradeep Kumar G., G. M. Kartha, A. M. Giri, and Gayathri V. for technical support. **Funding:** This work was supported by the Wellcome Trust/DBT India Alliance Fellowship (IA/I/15/2/502061); extramural grant from Department of Biotechnology, Government of India (BT/PR30459/MED/31/449/2021) awarded to S.K.; and intramural funds from Indian Institute of Science Education and Research Thiruvananthapuram (IISER TVM). IISER TVM Institutional animal facility is supported by funds from the Department of Science and Technology, Government of India (under FIST scheme; SR/FST/LS-II/2018/217). A.P.V. is supported by Senior Research Fellowship from the Department of Biotechnology, India. S.H.M. is supported by IISER TVM. M.T.A. is supported by the UAE University internal research grants (startup grant code G00003688 and UPAR grant code G00004152). C.M.V. is supported by funds from KU Leuven (IDO/13/016 HSC-Niche) and FWO (G0E0117N). **Author contributions:** A.P.V. established methods, planned and performed the experiments, performed statistical analysis, analyzed the data, and assisted in developing the manuscript draft. S.H.M. planned and performed proteomics based experiments, established the methods, developed bioinformatics pipeline, performed analysis, and assisted in developing the draft of the manuscript. C.M.V. reviewed the concept of the project, provided material support, and reviewed the manuscript. M.T.A. assisted in developing bioinformatics pipeline, supervised computational analysis of the proteomics data, and provided critical review of the manuscript. S.K. conceptualized the study; conceived, designed, and supervised all the experiments; raised funding and other resources; managed the project; analyzed the data; and wrote the manuscript. **Competing interests:** The authors declare that they have no competing interests. **Data and materials availability:** All data needed to evaluate the conclusions in the paper are present in the paper and/or the Supplementary Materials. The proteomics data, including the acquired raw files and the software search results, have been deposited to the ProteomeXchange Consortium (*53*) with the dataset identifier PXD042649 via the MassIVE partner repository (*54*) with the dataset identifier MSV000092085.

Submitted 29 June 2023
Accepted 17 January 2024
Published 16 February 2024
10.1126/sciadv.adh8478